

MARTA BERHOLTS

Fragmentation of ionic and
hydrogen-bonded molecules induced
by synchrotron radiation



Turun yliopisto
University of Turku



MARTA BERHOLTS

Fragmentation of ionic and
hydrogen-bonded molecules induced
by synchrotron radiation



UNIVERSITY OF TARTU
Press

This thesis was done under joint supervision of the University of Tartu (Institute of Physics, Faculty of Science and Technology, Estonia) and the University of Turku (Department of Physics and Astronomy, Faculty of Science and Engineering, Finland).

The dissertation is accepted for the commencement of the degree of Doctor of Philosophy in Materials Science on 18.06.2018 by the Council of Materials Science of the University of Tartu and on 15.06.2018 by the Faculty Council of the Turku University.

Supervisors: Prof. Edwin Kukk, Department of Physics and Astronomy, University of Turku
Prof. Ergo Nõmmiste, Department of Physics, University of Tartu
Ph.D. Kuno Kooser, Department of Physics and Astronomy, University of Turku

Reviewers: Prof. Jan-Erik Rubensson, Department of Physics and Astronomy, Uppsala University
Assoc. Prof. Matjaž Žitnik, Department of Low and Medium Energy Physics, Jožef Stefan Institute

Opponent: Assoc. Prof. Paolo Piseri, Department of Physics, University of Milan

Defense: 07.09.2018 at the University of Tartu, Tartu, Estonia

The originality of this thesis has been checked in accordance with the University of Turku quality assurance system using the Turnitin OriginalityCheck service.

This work was financially supported by graduate school “Functional materials and technologies” receiving funding from the European Social Fund under project 1.2.0401.09-0079 in Estonia and Internationalization Program DoRa (Foundation Archimedes).



DoRa



ISSN 2228-0928

ISBN 978-9949-77-799-0 (Print)

ISBN 978-9949-77-800-3 (Pdf)

Copyright © Marta Berholts, 2018

University of Tartu Press, www.tyk.ee

Abstract

In this work, we investigated experimentally and computationally the fragmentation processes of ionic and hydrogen-bonded molecules following valence photoionization. Four samples were studied: ionic 1-ethyl-3-methylimidazolium tetrafluoroborate (EMImBF_4) and hydrogen-bonded molecular clusters of acetamide (CH_3CONH_2), acetamide-2,2,2-d₃ (CD_3CONH_2), and acetic acid (CH_3COOH).

The goal of the work was to investigate the influence of the photon energy on the stability of the samples and their fragmentation mechanisms. Tunable synchrotron radiation or gas discharge lamp radiation in the vacuum ultraviolet region was used to ionize the molecules in the gas phase. Clusters were studied by mass spectrometry, while ionic liquid was additionally studied by photoelectron spectroscopy. Partial ion yield technique was used to elucidate the energetics of various photofragmentation pathways.

Both types of compounds were shown to be unstable toward near threshold ionization and therefore subjected to extensive fragmentation. Different fragmentation mechanisms were identified, and common trends in dissociation behaviour of ionic and hydrogen-bonded compounds were observed.

A significant finding is that not only photon energy influences the outcome of the valence ionization (at higher photon energy new fragmentation channels open up), but also the conditions at which the samples are introduced into the gas phase. In the case of acetic acid clusters, different clustering conditions resulted in different mass spectra. A conclusion is drawn that photofragmentation channels of a molecule depend on its internal energy. Lower internal energy suppresses atomic rearrangements that might be required for a certain fragment formation and instead, a new fragment is formed that does not require any rearrangement of the system. We observed such behaviour for acetic acid trimer that starts producing unprotonated dimers at stronger expansion conditions (lower internal energy), while there were no unprotonated dimers produced at weaker expansion conditions (higher internal energy).

Tiivistelmä

Tässä työssä tutkittiin kokeellisesti ja laskennallisesti ionisten ja vetysidottuneiden molekyylien pirstoutumisprosesseja valenssikuvan jälkeen. Tutkimuksessa tutkittiin neljä näytettä: ioninen 1-etyyli-3-metyyli-imidatsoliumtetrafluoriboraatti (EMImBF_4) ja sitovia molekyyliä (CH_3CONH_2), asetamidi-2,2,2-d₃ (CD_3CONH_2) ja etikkahappo (CH_3COOH).

Työn tavoitteena oli tutkia fotonien vaikutusta näytteiden vakauteen ja niiden hajotusmekanismeihin. Viritettävää synkrotronisäteilyä tai kaasupurkauslamppu säteilyä tyhjiö-ultraviolettialueella käytettiin molekyylien ionisoimiseen kaasufaasissa. Klustereita tutkittiin massaspektrometrialla, kun taas ionisoitua nestettä tutkittiin lisäksi fotoelektronispektroskopialla. Osittaista ionien tuotosmenetelmää käytettiin erilaisten valokuvaprosessointiväylien energioiden selvittämiseen.

Kummankin tyyppisten yhdisteiden osoitettiin olevan epästabiileja lähelle kynnysionisaatiota kohti, ja siksi ne olivat alttiita laajalle fragmentaatiolle. Eri pirstoutusmekanismit tunnistettiin ja havaittiin yleisiä suuntauksia ionisten ja vetysidottujen yhdisteiden dissosiaatiokäyttäytymisessä.

Merkittävä havainto on se, että valon ionisaation lopputulos ei vaikuta pelkästään fotonin energiaan (korkeammissa fotonien energiassa avautuu uudet fragmentaatiokanavat), vaan myös olosuhteet, joissa näytteet otetaan kaasufaasiin. Etikkahappokeskittymien tapauksessa erilaiset klusterointiolosuhteet johtivat erilaisiin massaspektreihin. Johtopäätös on, että molekyylin valokuvakehityskanavat riippuvat sen sisäisestä energiasta. Alhaisempi sisäinen energia heikentää atomien uudelleenjärjestelyjä, joita saatetaan tarvita tietyn fragmentin muodostumiselle, ja sen sijaan muodostuu uusi fragmentti, joka ei edellytä järjestelmän uudelleenjärjestelyä. Olemme havainneet tällaisen käyttäytymisen etikkahapon trimeerille, joka alkaa tuottaa ennalta protonoituneita dimeerejä voimakkaammissa paisumisolosuhteissa (alempi sisäinen energia), kun taas heikommilla laajentumisolosuhteilla (korkeampi sisäinen energia) ei tuotettu protoniittomia dimeerejä.

Contents

List of abbreviations	8
List of original publications	9
1 Introduction	11
2 Photofragmentation of molecules	14
2.1 Solving the structure of molecules	14
2.2 Ionization, excitation and fragmentation	17
3 Experimental background	20
3.1 Gas-discharge lamp	20
3.2 Synchrotron	21
3.2.1 Beamlines	24
3.3 Experimental techniques	27
3.3.1 Time-of-flight mass spectrometry	27
3.3.2 Partial ion yield technique	30
3.3.3 Photoelectron spectroscopy	30
3.4 Sample preparation	33
3.5 Adiabatic expansion and cluster formation	34
3.6 Data analysis	35
4 Results and conclusions	38
4.1 Ionic liquids	38
4.1.1 Mass spectrum of EMImBF ₄ : Observed fragments .	40
4.1.2 Possible photofragmentation pathways of EMImBF ₄	41
4.1.3 Thermal degradation	45
4.1.4 Electronic structure of EMImBF ₄	46
4.2 Clusters	51
4.2.1 Photofragmentation pathways	52
4.2.2 Proton transfer reactions	54
4.2.3 Formation of ammoniated acetamide clusters	56
4.2.4 Photofragmentation depending on the clustering condition	59
Conclusions	62
Summary in Estonian	64
Acknowledgements	66
References	67
Original papers	75

List of abbreviations

AE	Appearance Energy
B3LYP	Becke three-parameter Lee-Yang-Parr
DFT	Density Functional Theory
DOS	Density of States
EMIImBF ₄	1-ethyl-3-methylimidazolium tetrafluoroborate
HF	Hartree-Fock
HOMO	Highest Occupied Molecular Orbital
IE	Ionization Energy
IL	Ionic Liquid
LUMO	Lowest Unoccupied Molecular Orbital
M06	Minnesota 06 functional
MO	Molecular Orbital
MP2	Møller-Plesset perturbation theory of the second order
PIY	Partial Ion Yield
Tf ₂ N	bis[(trifluoromethane)sulfonyl]imide
TOF	Time-of-Flight
VUV	Vacuum Ultraviolet

List of original publications

This thesis includes the following research papers, which will be further referred to in the text by their Roman numerals:

- I. I. Kuusik, M. Tarkanovskaja, J. Kruusma, V. Reedo, R. Välbe, A. Lõhmus, V. Kisand, E. Lust, E. Kuk, and E. Nõmmiste. Near threshold photodissociation study of EMIMBF₄ vapor. *RSC Advances*, 5(9):6834-6842, 2014.
- II. I. Kuusik, M. Tarkanovskaja, J. Kruusma, V. Kisand, A. Tõnisoo, E. Lust, E. Nõmmiste. Valence band photoelectron spectra of [EMIM][BF₄] ionic liquid vapor: Evidences of electronic relaxation. *Journal of Molecular Liquids*, 223:939-942, 2016.
- III. M. Tarkanovskaja, K. Kooser, H. Levola, E. Nõmmiste, E. Kuk. Photoinduced intermolecular dynamics and subsequent fragmentation in VUV-ionized acetamide clusters. *The Journal of Chemical Physics*, 145(12):124313, 2016.
- IV. M. Berholts, H. Myllynen, K. Kooser, E. Itälä, S. Granroth, H. Levola, J. Laksman, S. Oghbaee, B. Oostenrijk, E. Nõmmiste, E. Kuk. Photofragmentation of gas-phase acetic acid and acetamide clusters in the vacuum ultraviolet region. *The Journal of Chemical Physics*, 147(19):194302, 2017.

The above-listed papers are the result of teamwork. In every paper, the author participated in the experimental measurements performed in MAX-Lab (beamlines I3 and I411) and at the Materials Research Laboratory of the University of Turku. The author was also responsible for the data analysis and creation of figures in papers I, III and IV. In paper I and II, the author was responsible for correcting and improving the written manuscripts. In papers III and IV, the author was responsible for writing the manuscript and corresponding author duties in the peer review process.

In addition, during the doctoral studies, the author was involved in the following publications that are not included in this thesis:

1. R. Välbe, R. Lõhmus, U. Mäeorg, M. Umalas, V. Reedo, M. Tarkanovskaja, A. Lõhmus, J. Kübarsepp. A method for preparing metal oxide nanoparticles in a gel. Patent number: EE 201500022 A; Priority date: 18.06.2014.
2. M. Tarkanovskaja, R. Välbe, K. Põhako-Esko, U. Mäeorg, V. Reedo, A. Hoop, K. Saal, A. Krumme, I. Kink, I. Heinmaa, and A. Lõhmus. Novel homogeneous gel fibers and capillaries from blend of titanium

- tetrabutoxide and siloxane functionalized ionic liquid. *Ceramics International*, 40(6):7729–7735, 2014.
3. R. Vålbe, M. Tarkanovskaja, U. Mäeorg, V. Reedo, A. Hoop, I. Kink, A. Lõhmus. Elaboration of hybrid cotton fibers treated with an ionogel/ carbon nanotube mixture using a sol-gel approach. *Open Chemistry*, 13(1):279–286, 2014.
 4. H. Levola, E. Itälä, K. Schlesier, K. Kooser, S. Laine, J. Laksman, D. T. Ha, E. Rachlew, M. Tarkanovskaja, K. Tanzer, and E. Kukk. Ionization-site effects on the photofragmentation of chloro- and bromoacetic acid molecules. *Physical Review A*, 92(6):063409, 2015.
 5. C. Siimenson, M. Lembinen, O. Oll, L. Läll, M. Tarkanovskaja, V. Ivaništšev, L. Siinor, T. Thomberg, K. Lust, E. Lust. Electrochemical Investigation of 1-ethyl-3-methylimidazolium bromide and tetrafluoroborate mixture at Bi(111) Electrode Interface. *Journal of the Electrochemical Society*, 163(9):H723–H730, 2016.
 6. R. Vålbe, M. Tarkanovskaja, U. Mäeorg, V. Reedo, A. Lõhmus, T. Taaber, S. Vlassov, R. Lõhmus. Phosphonium-based ionic liquids mixed with stabilized oxide nanoparticles as highly promising lubricating oil additives. *Proceedings of the Estonian Academy of Sciences*, 66(2):174–183, 2017.
 7. S. Oras, S. Vlassov, M. Berholts, R. Lõhmus, K. Mougin. Tuning adhesion forces between functionalized gold colloidal nanoparticles and silicon AFM tips: role of ligands and capillary forces. *Beilstein Journal of Nanotechnology*, 9(1):660–670, 2018.

1 Introduction

Electromagnetic radiation continues to be an essential tool in our exploration and understanding of the world. It all began with the visible light that we constantly use to see things around us with our eyes. Later on, scientific advances led to the exploitation of the radiation from the whole spectrum towards which our eyes are not sensitive, *i.e.* the wavelengths that are shorter or longer than the visible light. For example, long radio waves and microwaves are used in astronomy to study objects located far away from our planet, while infrared, ultraviolet and x-ray radiation are the best for examining the structure of the solid, liquid and gaseous samples. The shortest gamma rays go deeper and probe the inner structure of atoms. Different radiation wavelengths enable studying various processes on the basis of light-matter interactions.

Nowadays, one of the most powerful radiation sources is synchrotron accelerator. In a synchrotron storage ring, bright electromagnetic radiation in the range from infrared to x-rays is produced by electrons or positrons which are travelling close to the speed of light. In this thesis, we will concentrate on fragmentation processes induced by vacuum ultraviolet (VUV) radiation. According to ISO standard ISO-21348 [1], VUV radiation corresponds to wavelengths in the range of $10 \text{ nm} \leq \lambda < 200 \text{ nm}$ that is $6.2 - 124 \text{ eV}$, though the defined spectral region varies in the literature and is often given approximately from 10 to 100 eV. VUV studies involve valence electrons that are responsible for chemical bonding.

Comprehension and prediction of the photoinduced phenomena (*e.g.* ionization, molecular rearrangements, atomic motion, charge migration, bond fragmentation) at molecular level is highly important for understanding a large number of processes related with health problems (UV radiation-induced damage), technological challenges (photovoltaics, photosynthesis), and environmental studies (atmospheric photochemistry) among others. In this thesis, we studied experimentally and computationally the fragmentation processes induced by VUV synchrotron radiation in two different types of molecular systems: ionic liquid (IL) and molecular clusters. In particular, the following molecules were studied: 1-ethyl-3-methylimidazolium tetrafluoroborate or EMImBF₄, acetamide clusters and acetic acid clusters. In the cluster studies, the emphasis was put on the dimers. The structures of studied samples are presented in Figure 1, featuring the most stable structures of molecular dimers.

IL and molecular dimers are different by the nature of chemical bonding. Both compounds are overall neutral molecules and can be thought of as the systems composed of two counterparts. In IL, the counterparts (cation and anion) are held together by an ionic bond. Whereas in molecular dimers,

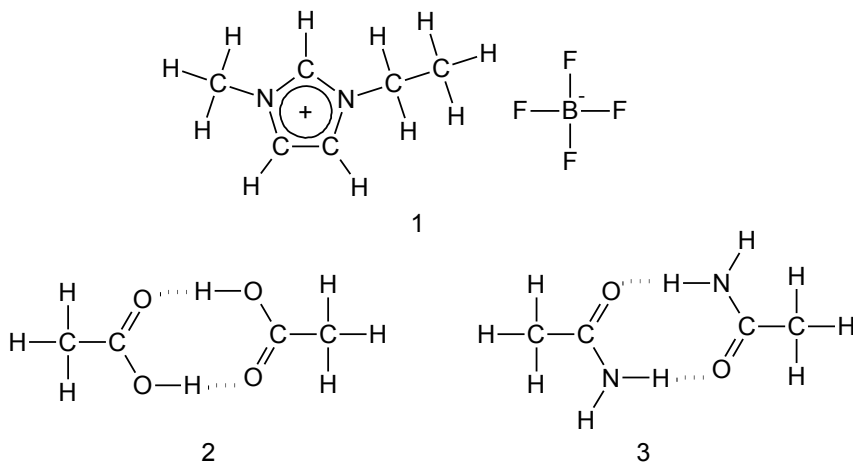


Figure 1: The molecules studied: (1) 1-ethyl-3-methylimidazolium tetrafluoroborate, (2) acetic acid dimer, (3) acetamide dimer.

the counterparts (two monomer subunits) are held together by hydrogen bonds. The ionic bond, in essence, is the electrostatic attraction between the oppositely charged ions. The hydrogen bond forms when a hydrogen atom attached to a strongly electronegative atom by a covalent bond also interacts electrostatically with the lone pair of another electronegative atom of another molecule.

Both ILs and clusters are diverse classes of compounds that might take on different structures and compositions. Studying interactions of ILs and molecular clusters with ionizing radiation gives valuable insights into the electronic structure and dissociation dynamics of these compounds.

A powerful tool to analyze neutral molecules by ionizing them and then separating them in space or time by their molecular weight is mass spectrometry. Ions can easily be guided, focused and separated by electric and/or magnetic fields, and, finally, detected. Combination of mass spectrometry with tunable synchrotron radiation allows exploring not only molecular dynamics and dissociation processes but also the energetics of different fragmentation pathways. Another widely used method is photoelectron spectroscopy, where not ions but emitted electrons are recorded that provide an image of the energy levels of the molecular orbitals in the photoionized molecule. Photoelectron spectroscopy has a substantial impact on quantum chemistry in terms of the development of advanced molecular calculations.

The goal of this work was to apply the above-mentioned experimental methods in combination with quantum mechanical calculations to study

the interactions of IL and cluster compounds with VUV photons and to characterize their properties on a molecular level. First, the influence of the photon energy on the stability of the samples and their fragmentation mechanisms was systematically investigated. This enabled to identify different fragmentation mechanisms and common trends in dissociation behaviour of ionic and hydrogen-bonded compounds. Second, the influence of the clustering conditions on the cluster size distribution and their photofragmentation pathways was examined. This resulted in a significant finding that the conditions at which the samples are introduced into the gas phase might influence the outcome of the photoionization.

This thesis is organized as follows: the introductory chapter is followed by chapter 2 and chapter 3 that provide an overview of the physics and techniques relevant to the research, correspondingly, then in chapter 4, the results of the thesis-included papers are summarized and discussed, after that, the main conclusions of the work are presented, followed by the summary of the work in Estonian.

2 Photofragmentation of molecules

In this section, the structure of the molecules will be explained as it is understood in terms of molecular orbital theory. Also, the computational methods used in this work will be briefly described. After that, light-matter interaction processes such as photoionization and photoexcitation that might lead to the decomposition of the molecule into fragments will be discussed.

2.1 Solving the structure of molecules

The molecules are composed of a number of atoms and have a definite geometric configuration. Atom is made up of a positive nucleus that is surrounded by one or more negative electrons orbiting around it. According to Born-Oppenheimer approximation, the atomic nuclei in the molecule could be considered as almost stationary compared to electrons [2]. It makes the calculations of electronic properties of molecules easier, allowing to separate the motion of electrons and nuclei. It is a reasonable assumption – proton (the nucleus of a hydrogen atom) is about two thousand times heavier than an electron. Therefore, nuclei define the geometry of the molecule.

The description of how atoms are held together in a molecule can only be obtained by quantum mechanical methods [3]. Most of the computational methods are based on or oriented toward the molecular orbital (MO) theory approach [4]. It is possible to calculate the probability of finding the electron at any point in the molecule by solving the molecular time-independent Schrödinger equation:

$$\hat{H}\Psi = E\Psi, \tag{1}$$

where \hat{H} is the Hamiltonian operator, Ψ is the wave function of the system, and E is the energy of the system. However, this equation can be solved exactly only for one-electron systems, while the exact solution for multi-electron systems is impossible due to electron-electron repulsion potential. Therefore, approximations are needed for molecules with more than one electron.

A common approach to constructing the wave functions for the Schrödinger equation is to use the linear combination of atomic orbitals (LCAO) approximation. The LCAO approximation starts with the wave functions χ_i localized on individual atoms (atomic orbitals) and combines them in various trial combinations. Obtained combinations are called

molecular orbitals ψ_m :

$$\psi_m = \sum_{i=1}^n c_{im} \chi_i, \quad (2)$$

where c_{im} is linear coefficient describing the contribution of the atomic orbitals to the molecular orbital. The number of formed molecular orbitals equals the number of atomic orbitals mixed.

The obtained molecular orbitals are the approximate solutions to the electronic part of molecular Schrödinger equation. The question remains, however, how to identify the best coefficients to obtain more accurate wave functions. Quantum-mechanical computational methods are dealing with this problem. For example, Hartree-Fock self-consistent field (HF SCF) method is an iterative process that calculates the energy of the system from initial guesses of molecular orbital coefficients until the energy is minimized and the best coefficients are acquired. For more detailed mathematical explanations of the method the readers are referred to Ref. [3] and [4].

The main problem of SCF methods is that they do not treat the electron-electron correlation properly, *i.e.* an electron moves in an electrostatic field produced by the average potential from other electrons. Correlation is important for improving the accuracy of computed energies and molecular geometries. Correlation is better accounted for in post-HF methods such as the Møller-Plesset method of the second order (MP2) used in this work. Here, electron interaction energy is lowered by allowing electrons to occupy formally unoccupied molecular orbitals.

One computational method that includes electron-electron correlation in its theoretical basis is called density functional theory (DFT) [4]. This method is based on Hohenberg-Kohn theorems, which postulate that the ground-state properties of the molecules and atoms are determined by their electron density function and that guessed electron density must give an energy greater or equal to the real energy. However, the second point is true only when the exact density functional is used, but the exact functional is not known, and since approximations are used, DFT can give energy values below the real energy, contrary to the HF method [4]. Among the popular functionals to approximate the exchange-correlation functional in DFT are B3LYP (Becke three-parameter Lee-Yang-Parr) and new functionals like Minnesota functionals of M06 family, both of which were used in this work.

One example of molecular orbitals calculated with HF method is presented in Figure 2. Here, the highest occupied molecular orbital (HOMO) and two orbitals below the energy of the HOMO are shown for acetic acid and acetamide dimer molecules. These molecular orbitals show that the electrons do not belong to individual bonds between two specific atoms but can extend over several atoms. Molecular orbitals are mathematical functions of the three spatial coordinates. Due to the

difficulty of illustrating such functions, isosurface plots (like in Figure 2) at a chosen wave function value are used for plotting them. Strictly speaking, the integer orbital-occupation numbers 0, 1 and 2 are only valid at the basic level of HF theory.

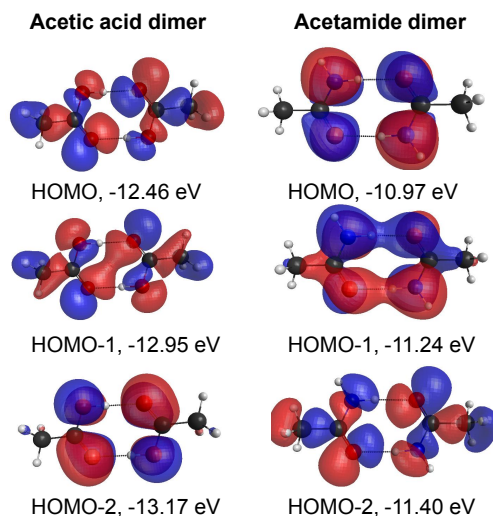


Figure 2: Molecular orbitals of acetic acid and acetamide dimers calculated with HF method: highest occupied molecular orbital (HOMO) and two MO that are lower in energy (HOMO-1 and HOMO-2). The blue regions are wave functions with a negative sign, the red ones are with a positive sign.

There are several types of molecular orbitals. Since atomic orbitals are wave functions, when combined they can interfere constructively forming a bonding orbital or destructively forming an anti-bonding molecular orbital. The bonding molecular orbital has lower energy than two separate atomic orbitals, while the anti-bonding orbital is of higher energy.

Molecular orbitals are formed when atomic orbitals with similar energies and proper symmetry can overlap. Atomic valence orbitals that do not participate in the formation of molecular orbitals are called non-bonding orbitals. Deep inner shell orbitals remain essentially atomic since their overlap with the orbitals on other atoms is negligible. There are also unoccupied molecular orbitals that are located above valence orbitals and are higher in energy. The lowest unoccupied molecular orbital (LUMO) and the HOMO are separated by a gap. LUMOs can accept electrons from lower occupied orbitals or from neighbouring molecules or atoms. As is shown in Figure 2, HOMOs, which contain highest-energy electrons, can

extend over multiple atoms of a molecule due to the strong interaction of valence atomic orbitals. The lowest-energy electrons are concentrated close to the nucleus on core orbitals and are localized around a certain atom. Therefore, electrons of the valence orbitals could be considered as the ones responsible for the formation of chemical bonds.

2.2 Ionization, excitation and fragmentation

The energies of molecular orbitals can be determined experimentally by photoelectron spectroscopy. This method relies on photoelectric effect that was first observed by Heinrich Hertz in 1887 [5] and explained later in 1905 by Albert Einstein [6]. The effect is based on an ionizing interaction of radiation with matter. When energy is given to a molecule, a quantum mechanical transition from the ground state, the lowest energy state of the molecular system, to a more energetic state can occur.

In a photoionization process, a cation M^+ is formed as a result of interaction of photons of sufficient energy ($E = h\nu$, where $h \approx 6.63 \times 10^{-34} \text{J}\cdot\text{s}$ is Planck constant and ν is the frequency of radiation) and a neutral molecule M :



Upon the ionizing absorption of a photon by the molecule, the electron is emitted into the continuum as shown on the left-hand side of Figure 3. This electron has a kinetic energy (E_{kin}) that corresponds to the difference between the photon energy and the binding energy (E_{bin}) of the electron in accordance with the law of conservation of energy:

$$E_{kin} = h\nu - E_{bin}, \quad (4)$$

The minimum amount of energy required to emit the electron from the highest occupied molecular orbital is called ionization energy. Formation of a positive ion is possible for any photon energy above the ionization energy. Depending on photon energy, an electron can be removed from core or valence orbitals or excited to initially unoccupied molecular orbital. By measuring the kinetic energy of the emitted electrons, it is possible to determine their binding energies, thus, in Koopmans' approximation also the energies of the molecular orbitals [7]. Koopmans' theorem postulates that the ionization energy required to remove an electron from the orbital is given by the negative value of the energy of the orbital [7].

Figure 3 depicts photoionization and photoexcitation (also called resonant excitation) processes with valence electrons involved. We consider only valence electrons because this thesis deals with VUV radiation that has not enough energy to remove the core electrons. In a resonant

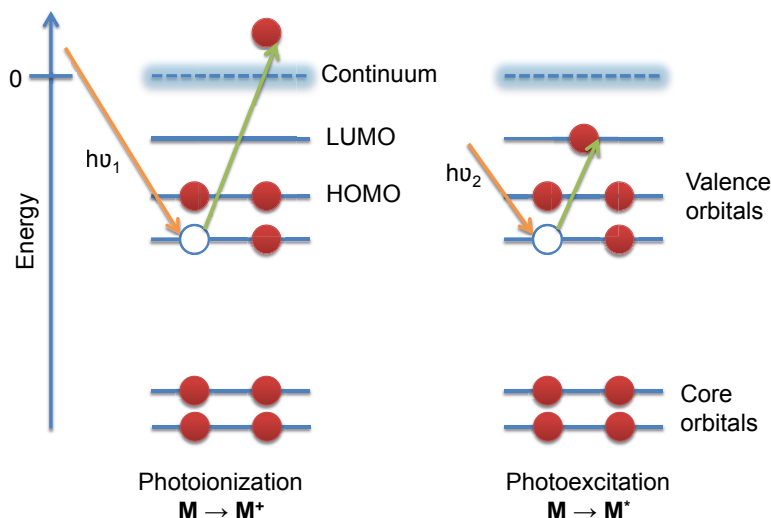


Figure 3: Photoionization and photoexcitation of the valence orbitals. Red dots are electrons, and white dots are vacancies created by the absorption of a photon. Photon energy $h\nu_1$ is greater than $h\nu_2$.

excitation process, the energy of the photon has to fulfill the condition:

$$h\nu = E_1 - E_2, \quad (5)$$

where E_1 is the binding energy of the molecular orbital from which electron is promoted and E_2 is the binding energy of the orbital that accommodates this electron.

Photoionization and photoexcitation result in the formation of a more energetic and thus less stable state of the molecule. To achieve stabilization, the reorganization of the orbitals and energies of the electrons might occur. Therefore, when a molecule is excited or ionized, it may possess high internal energy that is capable of breaking the molecule apart. The process is called fragmentation. If fragmentation happens due to irradiation of a sample with photons, it is called photofragmentation and resulting fragments – photofragments. The minimum energy required to create a molecular fragment is called appearance energy of the fragment. If created molecular ion or excited molecule contain sufficient internal energy, they may undergo various competing dissociation reactions, leading to the breakage of the molecule at different sites.

Dissociative photoionization and photoexcitation are very important processes in the VUV region. Mass spectrometry is an excellent tool to get more insight into VUV photochemistry as it is capable of detecting

all the ions that are created in these processes. However, to differentiate or eliminate some of the possible fragmentation pathways, the quantum chemical calculations are often necessary. Therefore, calculations play an essential role in the determination of possible outcomes of the photoionization and photoexcitation processes. The analysis of reaction energetics can predict what kind of molecular processes are able to occur or likely to occur.

3 Experimental background

In this thesis work, the gas-phase samples were studied by vacuum-ultraviolet (VUV) spectroscopic methods. These methods investigate the outcome of the light-matter interactions in the VUV region (approx. 10-100 eV). Various product particles such as electrons, photons, and ions that are created when sample is illuminated by VUV radiation are detected by different techniques. In this work, the ions were detected with time-of-flight mass spectrometry and electrons with photoelectron spectroscopy. For all compounds, partial ion yield (PIY) technique was used to determine the appearance energies of the fragments.

As a source of VUV photons, we used the radiation produced by a synchrotron or a gas discharge lamp. Electronic transitions involving valence electrons have energies that are in the range of VUV photons, which are hence useful as probes for the chemical nature and electronic properties of materials. Synchrotrons are designed to generate beams of high-intensity tunable electromagnetic radiation. The tunability of the synchrotron radiation makes it possible to choose different photon energies in the VUV range, while gas discharge lamps (another source of VUV light) does not have that option. On the other hand, discharge lamps are affordable, easy to handle, and are capable of producing very high light intensities at some resonance wavelengths.

In this work, the samples were introduced into the gas phase. IL was introduced via evaporation from a crucible located in a resistively heated oven. Cluster beams were generated by a continuous supersonic expansion source.

The next sections will describe the basic concepts of used radiation sources (gas discharge lamp, synchrotron) and experimental techniques (time-of-flight mass spectrometry, PIY technique, and electron spectroscopy). Also, some detail will be given on the sample preparation techniques.

3.1 Gas-discharge lamp

The gas-discharge lamp produces radiation by applying an electric discharge through an ionized gas (typically a noble gas such as argon used in this work). Generated radiation is coming from the gas that fills up a discharge capillary between the cathode and anode. The electrons emitted by the cathode accelerate toward the anode and thus gain the required energy in the electric field to excite or ionize the gas atoms upon collision. The excited atom can emit electromagnetic radiation in a relaxation process when the electron returns from higher energy state to the lower one.

The gas-discharge lamp used in this work is high-intensity VUV source (HIS 13) purchased from FOCUS GmbH. It achieves very high intensities by integrating a high voltage anode into the self-centering discharge capillary (see Figure 4). The lamp employs water cooling that makes high discharge currents (up to 300 mA) possible, reducing electrode degradation, and differential pumping to avoid excessive leakage of discharge gas into analysis chamber.

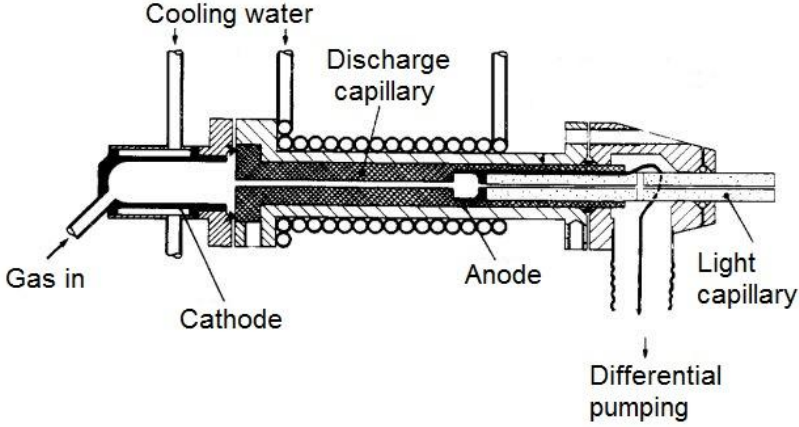


Figure 4: Schematics of a cold cathode gas-discharge lamp (adapted from [8]).

3.2 Synchrotron

The working principle of a synchrotron relies on the fact that accelerating charged particles (electrons or positrons) emit electromagnetic radiation [9, 10, 11].

From the first observation of synchrotron radiation in 1947 (described in Ref. [12]) to our time, more than 70 synchrotrons have been built around the world, each allowing for multidisciplinary research [13]. A schematic illustration of a typical synchrotron is presented in Figure 5. A modern synchrotron facility consists of 4 main components held under vacuum to minimize electron collisions with the rest gas molecules and to prevent absorption of the produced radiation. These components are discussed below with a short description of processes happening to the electrons and emitted electromagnetic radiation inside them:

1. *Linear accelerator or linac* accelerates electrons generated in the electron gun with high voltage. Linac incorporates an electron gun at one end (the cathode), and as the electrons are being released they

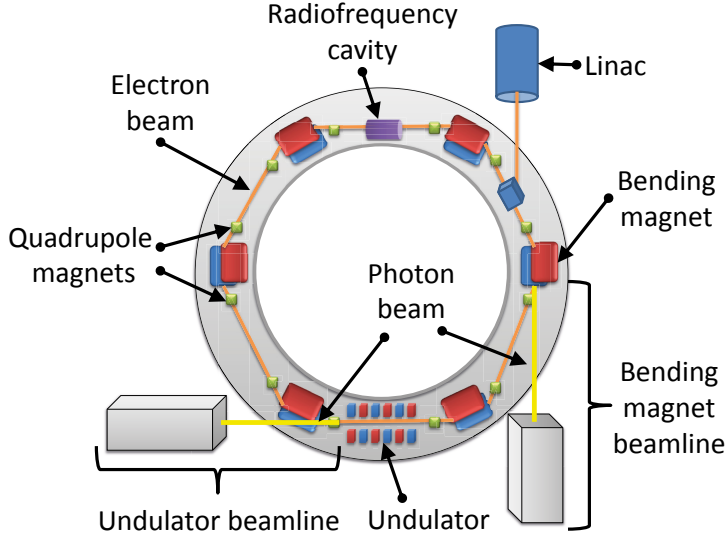


Figure 5: Schematic illustration of a synchrotron storage ring.

are directed to the positive anode located on the opposite end. In the centre of the anode is a small aperture that allows the electrons to pass through either into the booster ring that accelerates electron stream even further to the energy of electrons in main storage ring or less (commonly measured in GeV) or straight to the storage ring.

2. *Storage ring* stores the relativistic electrons inserted from the linac or the booster ring. Synchrotron light is produced in the storage ring. Around the storage ring, there are different kind of magnets, which force the electron beam to focus (quadrupole magnets), to bend (bending magnet), or to travel in a "snaking" path (undulator, wiggler). Inserted in the storage ring radiofrequency cavity supplies the electrons with the required amount of energy to compensate for the energy loss due to emitted radiation when electrons pass the above-mentioned magnetic structures.
3. *Beamlines* start after the magnetic structure and run off tangentially from the storage ring. Beamlines have many optical devices (filters, beam-position monitors, mirrors, lenses, monochromators, etc.) to control and improve the quality of the radiation produced by the electrons focusing, measuring and purifying the photon beam along its final path to the experimental chamber.
4. *Experimental end-stations* are used to perform the experiments as here radiation hits the sample placed in its path. Depending on the experiment, end-stations have different analyzing equipment.

For generation of synchrotron radiation, relativistic electrons are deflected transversely to their direction of motion by magnetic fields. Due to the relativistic velocity of the electrons, the radiation is emitted in a narrow cone along the direction of motion of the electrons.

Emitted radiation characteristics such as spectral width and radiation intensity depend on the electron deflection mode. As was mentioned above, there are three types of magnetic structures commonly used in synchrotrons to produce electromagnetic radiation: bending magnet, wiggler, and undulator. In a bending magnet (dipole magnet), electrons are forced to move in a circular motion in a constant magnetic field. The emission of synchrotron radiation as a narrow cone of radiation results from the centripetal acceleration of electrons travelling close to the speed of light. Wigglers and undulators (multipole magnets), on the other hand, use static magnetic field that oscillates in space. It is created by the structure of magnets separated by a gap that forces the electrons to move in a sinusoidal ("snake slithering") path in a transverse plane to the direction of electron motion. At every bend, a radiation cone is emitted. The schematic illustration of an undulator along with undulator radiation spectrum is presented in Figure 6. The difference between wiggler and

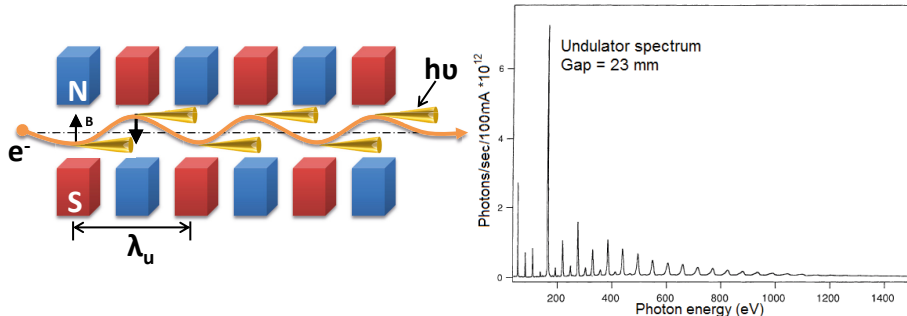


Figure 6: Schematic illustration of an undulator (left) and an undulator-produced radiation spectrum recorded at beamline I411 of MAX-II storage ring (right). The spectrum is adapted from Ref. [14].

undulator is in the degree to which the electrons are forced to deviate from a straight path. The nature of the electron movement in a periodic magnetic field is described by undulator/wiggler strength parameter:

$$K = \frac{eB\lambda_u}{2\pi m_e c}, \quad (6)$$

where e is the electron charge, B is the magnetic field, λ_u is the spatial period of the magnets, m_e is the rest mass of an electron and c is the speed of light.

In wigglers, $K \gg 1$ (stronger magnetic field), therefore the deviation from the straight path is higher which results in lower radiation intensities as the radiation cones from each bend do not overlap. In undulators, $K < 1$ (weaker magnetic field), therefore the amplitude of the electron path is smaller, and radiation cones emitted by the electrons overlap and interfere creating higher intensities upon constructive interference of certain wavelengths. As a result, undulator spectra consist of narrow bands of radiation (see the right-hand side of Figure 6), while the spectra of bending magnet and wiggler are continuous over a broad range of electromagnetic radiation.

The gap between upper and lower magnetic arrays is adjustable. Pushing the magnets closer to each other and increasing the magnetic field, the forces on the electron beam increase, forcing it to deviate more from a straight path. This change in curve produces the change in wavelength of the emitted radiation. The curves with the larger amplitude produce longer wavelength radiation, while the curves with the smaller amplitude produce shorter wavelength radiation. As a result, modern synchrotron light sources cover radiation wavelengths from the infrared to hard x-rays with superior brilliance¹ and high intensity. The modern synchrotrons equipped with undulators achieve brilliance values as high as 10^{21} photons/s/mrad²/mm²/0.1% BW. It is beneficial for ion and electron spectroscopies as the larger amount of photons ionizes more molecules and result in the stronger signal detected.

The polarization of the undulator radiation could be changed from linear (as shown in Figure 6) to circular or elliptical by APPLE-type (advanced planar polarized light emitter) undulator. This undulator consists of four magnetic arrays instead of two (two below and two above the electron beam). Longitudinally moving the two opposing magnetic arrays with respect to the fixed ones, the polarization of the radiation produced is varied, since a phase shift is created and the strengths of the vertical and horizontal magnetic field components are varied. Beamline I3 of MAX-III storage ring was APPLE-type undulator beamline. In our experiments, linear horizontally polarized radiation was used.

3.2.1 Beamlines

Measurements related with this thesis were performed at the undulator beamlines FINEST I3 [15, 16] of the 700 MeV MAX III storage ring (see

¹Brilliance shows how the photon flux [photons/s/0.1% BW] is distributed in space and angular range and is expressed as [photons/s/mrad²/mm²/0.1% BW] [13].

Figure 7 for the beamline layout) and I411 [17, 14] of the 1.5 GeV MAX II storage ring (see Figure 8 for the beamline layout) of former MAX-Lab synchrotron facility in Lund, Sweden. I3 beamline was designed for the

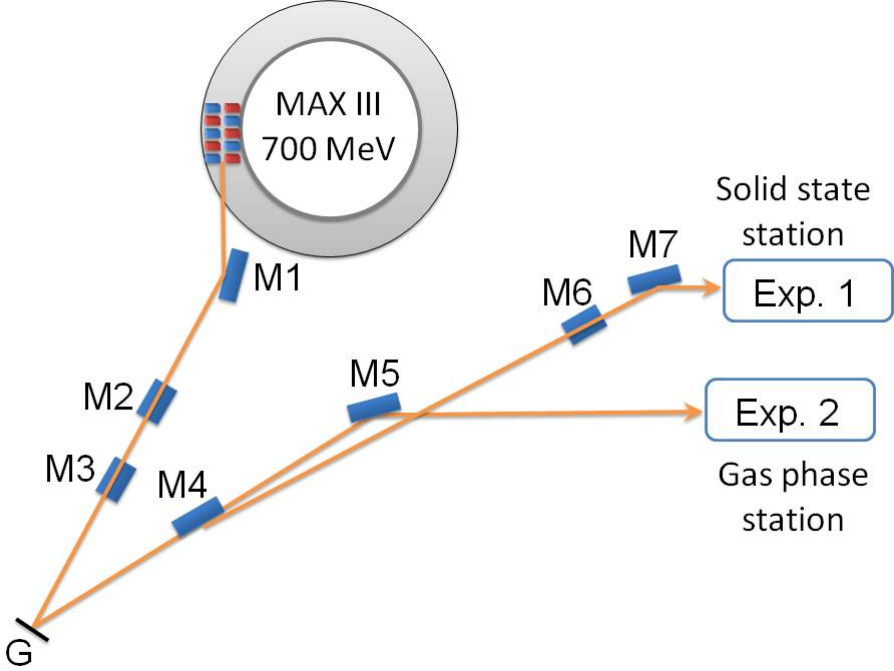


Figure 7: Schematic layout of I3 beamline at MAX III storage ring [15]. Pre-optics (mirrors M1, M2, and M3) focus the radiation on the monochromator grating (G). Post-optics (mirrors M4, M5, M6, and M7) compensate for the changing angle due to grating translation and focus the light to the experimental stations. M4 is also used to switch between the solid state (Exp. 1) and gas phase/luminescence (Exp. 2) stations.

low energy region of 5-50 eV. The beamline had two branches: one was mainly used for atomic and molecular spectroscopy and luminescence measurements and another for photoelectron spectroscopy on solids (see Figure 7). We used the gas-phase branch (Exp. 2 in Figure 7) that was equipped with a 6.65 m normal incidence monochromator allowing for maximum resolving power of $\approx 10^5$. The monochromator had three gratings for different energy regions: 2400 lines/mm MgF_2/Al coated grating for photon energies from 5 to 11 eV, 4300 lines/mm Pt-coated grating for photon energies above 26 eV, and a low-density 430 lines/mm Au grating for energies from 5 to 50 eV for high flux and medium resolution. The latter was used in the experiments with clusters, while

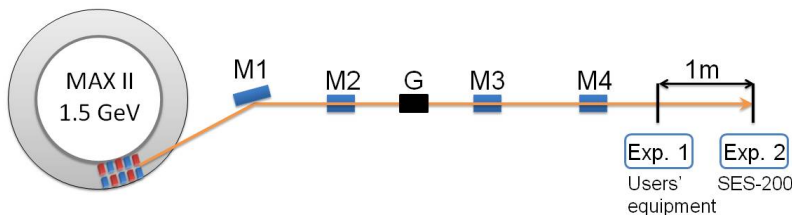


Figure 8: Schematic layout of I411 beamline at MAX II storage ring [14]. M1 is horizontally focusing mirror. Plane mirror M2 and focusing mirror M3 together with the plane grating G1 are the part of the Zeiss SX-700 monochromator. M4 is refocusing mirror. 1 m section of free space between Exp. 1 and Exp. 2 could be used to mount required equipment for a specific experiment. End-station Exp. 2 is equipped with Scienta SES-200 electron analyzer.

MgF₂/Al coated grating was used in the mass spectrometric measurements of ionic liquid.

Differential pumping stage between the beamline and the end-station provided the pressure difference in these regions and allowed for gas phase experiments without damaging the ultrahigh vacuum in the beamline. Photon flux on the sample was $10^{11} - 10^{13}$ ph/s/0.1%BW, spot size on sample was 0.3 mm (V) x 0.5 mm (H). During the measurements, the end-station was equipped with the analyzing equipment of the University of Turku – Wiley-McLaren-type time-of-flight mass spectrometer.

The soft x-ray undulator beamline I411 was designed for the energy region of 50-1500 eV. The beamline design was suitable for gaseous, solid, and liquid samples. The beamline was equipped with modified Zeiss SX-700 monochromator with 1220 lines/mm grating and a plane-elliptical focusing mirror, allowing for a resolving power of $10^3 - 10^4$. Photon flux on the sample was $10^{11} - 10^{13}$ ph/s/0.1%BW. During the measurements, the end-station was equipped with Scienta SES-200 hemispherical electron energy analyzer for photoelectron spectroscopy measurements.

3.3 Experimental techniques

3.3.1 Time-of-flight mass spectrometry

Before focusing on the operating principle of time-of-flight mass spectrometer, let's discuss the basic principle of mass spectrometry in general. The fundamental principle of mass spectrometry relies on three main aspects: Generation of gas-phase ions from compounds under study by any suitable method (*e.g.* photon or electron ionization), separation of those ions by their mass-to-charge ratio (m/z) using a mass analyzer (*e.g.* time-of-flight, quadrupole, magnetic sector analyzers), and detection of ions qualitatively and quantitatively by their m/z and abundance, respectively [18]. When $z = 1$ (*i.e.* ions are singly ionized) as is the case with near threshold ionization, the m/z scale directly reflects the m scale. In commonly used mass analyzers, ions are subjected to the electric or/and magnetic fields. The applied force to the ions can be presented by the Lorentz force law:

$$\vec{F} = ze\vec{E} + ze\vec{v} \times \vec{B}, \quad (7)$$

where \vec{F} is the force vector, z is the number of charges, $e = 1.6 \times 10^{-19}$ C is the elementary charge, \vec{E} is the electric field vector, \vec{v} is the ion velocity, and \vec{B} is the magnetic field vector. In the case of the nonmagnetic mass analyzer ($\vec{B} = 0$), the ions are influenced only by the electric force $\vec{F} = ze\vec{E}$. The ion with mass m_i in the electric field will have an acceleration \vec{a} according to the second law of motion if the potential difference exists:

$$\vec{a} = \frac{ze\vec{E}}{m_i}. \quad (8)$$

From the above equations, it is obvious that the acceleration depends both on the ion mass and the charge. Therefore, mass spectrometers do not separate the ions according to their mass but according to the ion m/z .

Next, we discuss the operating principle of Wiley-McLaren type linear time-of-flight (TOF) mass spectrometer used in this work. The advantages of TOF mass analyzers are high ion transmission, fastest analyzing speed, highest practical mass range, accurate mass measurements, good mass resolving power, compact design, and relatively low price. Wiley-McLaren TOF spectrometer's design was introduced in the 1950s allowing for significantly improved mass resolution [19] in comparison with its predecessors. The revolutionary design used two-stage acceleration of the ions by the two electric fields instead of the single acceleration. A schematic view of the two-field TOF spectrometer is presented in Figure 9. The key principle of TOF mass analyzer is to separate ions with different

m/z in time and to identify these ions by measuring the time required for the specific ion to reach the detector. The time of flight, T , of an ion is directly proportional to the square root of ion's m/z and is expressed as:

$$T = T_o + C\sqrt{\frac{m}{z}}, \quad (9)$$

where T_o and C are calibration constants that depend on the parameters of the spectrometer and could be calculated by solving the above equation for two known mass signals (*e.g.* rest gas ions always present in the vacuum chamber such as N_2^+ and H_2O^+). The typical flight times of the ions are in the order of microseconds.

The TOF spectrometer used in this work consists of three regions separated by the grids (see Figure 9). First, ions are formed in the ionization region by a photon impact. Then, generated ions are drawn out from the ionization region to the acceleration region by applying extraction voltages, V_s , in short high-voltage pulses (100-300 V) by a pulse generator. Pulse generator provides the starting signal to the timing electronics at each pulse. In the acceleration region, the ions with the same charge value are accelerated to the same kinetic energies by a constant electric field, E_d . After acceleration region, the ions enter the electric field-free region (also called drift tube) and continue moving toward the detector. According to Equation 9, the flight time of the ions is a function of their m/z . When an ion hits the detector, time measurement stops. If only singly charged ions are present, the lightest ions reach the detector first followed by the heavier ones (top of Figure 9). As an output, after every extraction pulse, one gets a mass spectrum of a sample where various peaks represent different ions.

Returning to the topic of the enhanced mass resolution in two-field TOF spectrometers in comparison to the one-field spectrometers, we must define what the resolution of a TOF mass spectrometer is. The ions created in the ionization region do not have the same kinetic energies and starting times, which makes it difficult to make narrow bunches of ions with the same m/z and prevent the widening of the peaks. Therefore, the overall resolution of a TOF spectrometer depends on its ability to reduce the time spread caused by initial kinetic energy and space distributions of the ions. Two-stage acceleration method prevents the spatial spread of the ions by a simple adjustment of the electric fields E_s and E_d by applying voltages V_s and V_d in the ionization and acceleration region of a spectrometer, correspondingly (see Figure 9). Consequently, the ions with the same m/z can reach the detector at the same time independently of their initial creation position (bottom of Figure 9). The specific ratio of E_s/E_d that results in the narrow ion bunches and therefore narrow mass peaks is called Wiley-McLaren

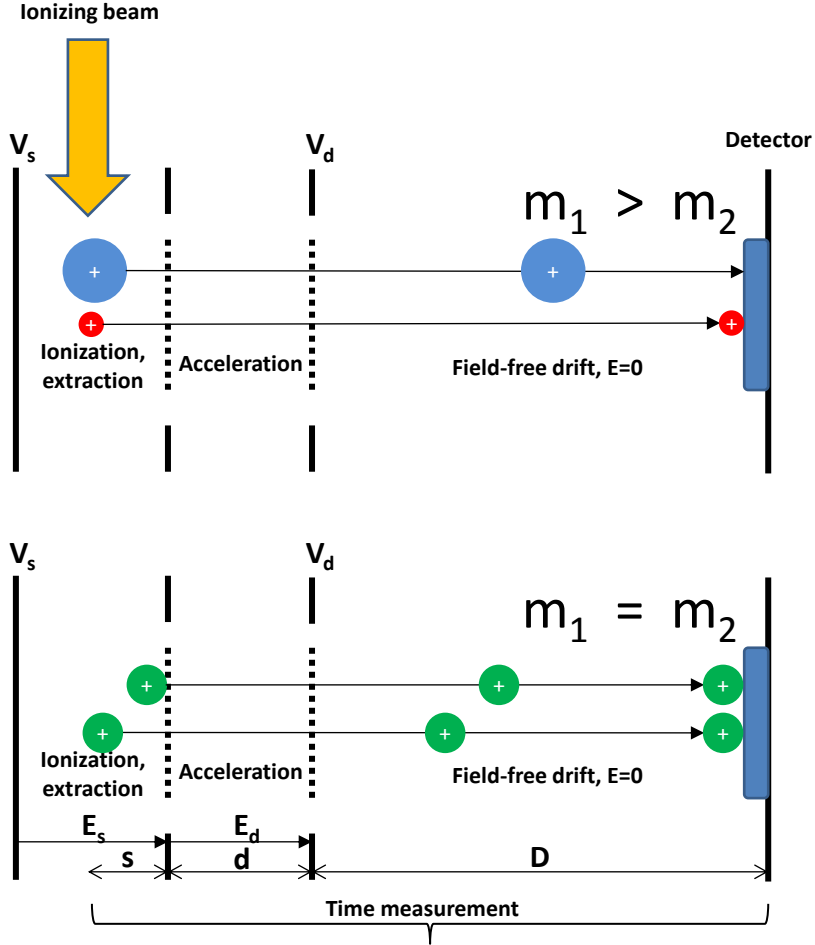


Figure 9: Schematic illustration of a Wiley-McLaren time-of-flight mass spectrometer. Top: Ions with different masses and the same initial position arrive at the detector at the different time. Bottom: Ions with the same mass and different initial positions arrive at the detector at the same time (space focusing).

space-focusing condition, D . D is the position in a drift tube, at which ions of the same m/z but different initial positions s_0 will pass each other. The focusing condition is calculated from

$$D = 2s_0k_0^{3/2} \left(1 - \frac{d}{s_0(k_0 + k_0^{1/2})} \right) [19], \quad (10)$$

where d is the length of the acceleration region and k_0 is defined by

$$k_0 = \frac{s_0 E_s + d E_d}{s_0 E_s}. \quad (11)$$

Therefore, when s_0 , d , and D are fixed, E_d/E_s is determined by Equation 10. In the single acceleration system, however, the focus condition could only be influenced by the spectrometer's geometry, $D = 2s_0$.

The mass spectrometer used in this work was equipped with an 80 mm active area diameter Hamamatsu microchannel plate (MCP) detector. MCPs consist of a large amount of fused together conductive glass capillaries (channels) and essentially are secondary electron multipliers. MCPs have a high-speed response and high ion detection efficiency required for mass spectrometric experiments.

3.3.2 Partial ion yield technique

The mass spectrum itself gives a lot of valuable information about the sample structure, composition and fragmentation abundance. However, partial ion yield (PIY) technique provides additional information about the appearance energies of the parent and fragment ions. In a PIY technique, the yield of a specific ion is counted as a function of photon energy. In practice, the PIY technique is realized by measuring an array of mass spectra at increasing photon energies. Subsequently, the ion yield curves are extracted by integrating the ion counts at every photon energy over the time window containing the selected ion peak and then plotting obtained intensities versus photon energy (for more details see subsection 3.6).

PIY technique requires a tunable radiation source. In this work, PIY experiments were performed at the undulator beamline, which allows quick tune of the photon energy by adjusting the undulator gap and tuning the monochromator.

3.3.3 Photoelectron spectroscopy

The heart of the photoelectron spectroscopy is the electron spectrometer. Electron spectrometer separates electrons, emitted from the sample by the photon impact, according to their kinetic energies and records electron energy distribution, *i.e.* counts how many electrons have a certain kinetic energy value. The kinetic energies of the photoelectrons are connected to their binding energies via $E_{kin} = h\nu - E_{bin}$. Therefore, the photoelectron spectrum gives the information about the energies of the molecular (or atomic) orbitals [20].

In this work, the most common electron spectrometer type was used

during the measurements – concentric hemispherical analyzer. It consists of three parts: a lens system, a hemispherical analyzing section and a detector as shown in Figure 10.

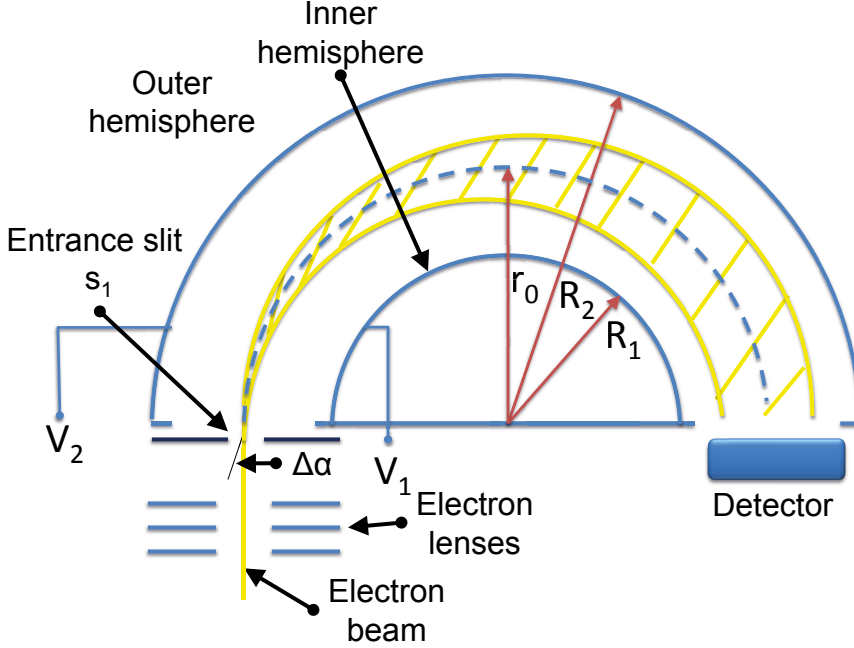


Figure 10: Schematic illustration of a concentric hemispherical electron energy analyzer.

Prior to the entering into the hemisphere, the electrons are focused, decelerated or accelerated by several electrostatic lenses to match the fixed kinetic energy value called pass energy, E_p . Therefore, not all electrons get to the detector but only those with specific kinetic energies around pass energy. To select which of the emitted electrons will obtain the chosen pass energy, suitable electron deceleration is applied. Thus, the lens system modifies the initial kinetic energies of the photoelectrons.

In the hemispherical section, electrons that are accelerated or decelerated exactly to pass energy move along a certain radius (often called the nominal radius of the analyzer, $r_0 = (R_1 + R_2)/2$, where R_1 and R_2 are the radii of the inner and outer hemisphere, respectively) between the two hemispheres (blue dashed line in Figure 10). The radius is determined by the selection of inner, V_1 , and outer, V_2 , electrode voltages, where V_1 is always at more positive potential than V_2 . The motion of the electrons in an electric field between the hemispheres at a

potential difference of $\Delta V = V_2 - V_1$ is described by Newton's second law and the Lorentz force. The electrons move along a curved trajectory with an electron's energy-dependent radius. Electrons will be focused at the detector along the nominal radius r_0 if

$$e\Delta V = E_p \left(\frac{R_2}{R_1} - \frac{R_1}{R_2} \right), \quad (12)$$

where e is the elementary charge.

Thus, the principle of the energy analysis is based on the dispersion of the electrons in a deflecting field. Electrons that have lower energy than the pass energy move closer to the inner hemisphere, while higher energy electrons move closer to the outer hemisphere. Subsequently, slow and fast electrons arrive at different positions on the detector, while too slow or too fast electrons collide with the electrodes and never reach the detector. The radial displacement of electrons with energy $E_p + \Delta E$ on the exit plane of the spectrometer is given by $\Delta r \sim 2r_0\Delta E/E_p$, valid for small entrance angle.

There are two modes of running the spectrometer [21]. In the first mode, the pass energy is kept constant, and the voltages of the electric lenses are scanned. As an example, in SES-200 instrument [22], the size of the kinetic energy range detected by the detector is around 10% of the selected pass energy. If one wants to measure electrons with 100 eV kinetic energy at a pass energy of 10 eV, a retardation potential of -90 eV should be applied to the electrons by the lenses. Thus, by scanning the retardation potential, an entire electron spectrum is recorded.

In the second mode, the pass energy is not constant, and the hemispherical electrodes' potential difference is scanned. In our experiments, we preferred the first mode because it gives constant resolution within an entire spectrum.

Two important parameters for the electron analyzer are the resolution (minimum energy difference between electrons that can be separated) and transmission (the effectiveness of the electron collection process, *i.e.* ratio of all the electrons created in the ionization to the detectable electrons). Resolution is related to the pass energy, entrance, s_1 , and exit, s_2 , slit widths and electron divergence, $\Delta\alpha$, according to

$$\frac{\Delta E}{E_p} = \frac{s_1 + s_2}{R_1 + R_2} + (\Delta\alpha)^2. \quad (13)$$

According to the above equation, lower pass energies and smaller slits result in better resolution. However, this worsens the transmission of the spectrometer, leading to the decrease of signal intensity. When a position sensitive detector is used, instead of the exit slit, the accuracy of the

detector (how well it can record the electron hit coordinates) is used to determine the resolution. In case of position sensitive detector, not only the resolution is improved, but also the signal intensity is increased since the electrons can be collected from the whole active surface of the detector.

In Scienta SES-200 electron analyzer, used in this work, the electrons are detected by MCPs-phosphor screen-charge-coupled device (CCD) detector system [22]. The electron avalanches coming from MCPs create spots of visible light on the phosphor screen, positions of which are recorded by a CCD camera.

3.4 Sample preparation

Samples studied in this work were in the form of liquids (acetic acid, 1-ethyl-3-methylimidazolium tetrafluoroborate) and powders (acetamide, acetamide-2,2,2-d₃). The acetamide, acetic acid and IL were purchased from Sigma-Aldrich, partly deuterated acetamide was purchased from Qmx Laboratories. To introduce the IL into the interaction region of the vacuum chamber in the form of single molecules, it was evaporated from a crucible located in the resistively heated oven (MBE Komponenten NTEZ40). The vapors of IL were then ionized and analyzed by mass spectrometry and electron spectroscopy.

To make gas-phase clusters from the acetic acid, acetamide and partly deuterated acetamide, home-made continuous supersonic cluster source was used. The source was designed and built by Dr. Kuno Kooser based on the construction reported by Kim *et al.* [23]. The schematic view of the experimental chamber containing a cluster source is presented in Figure 11. The solid samples had to be heated in an oven to obtain sufficient vapor pressure, while heating of the liquid acetic acid was not required as it has already high vapor pressure.

For the formation of clusters, the effusing vapor of the sample mixed with argon carrier gas in a nozzle containing reservoir expanded through the nozzle into the vacuum, from high-pressure region to low-pressure region. Adiabatic expansion and cooling resulted in the formation of clusters by condensation of the molecules. After expanding through the nozzle (in this work, converging custom-made quartz nozzles were used with diameters of 7 μm and 18 μm), the cluster beam passed into ionization chamber through a 2-mm skimmer. In ionization chamber, the generated clusters were ionized and then analyzed by time-of-flight mass spectrometry. The pressure of the expansion chamber was held at around 1.2×10^{-4} mbar, and the pressure of the ionization chamber was held at around 1.16×10^{-6} mbar.

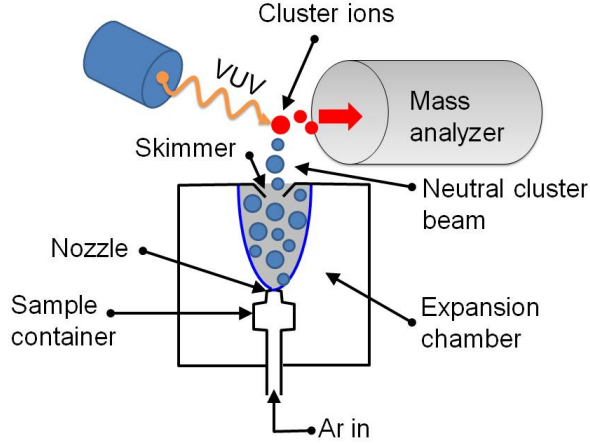


Figure 11: Schematic illustration of an experimental chamber for cluster formation, ionization and detection.

3.5 Adiabatic expansion and cluster formation

As a result of adiabatic (isentropic) expansion, the gas is emitted into a conical space angle that expands from the exit of the nozzle as schematically is shown in Figure 12 [24, 25]. The direction of the gas flow is however distributed and turned back into the center of the jet by pressure boundary conditions and shock waves around the expanding gas. The jet becomes compressed at the downstream from the nozzle. In this region, a Mach disk is formed (see Figure 12), and the pressure of the gas is significantly increased. Therefore, a skimmer must be placed before Mach disk to eliminate any disturbing effects on the cluster beam.

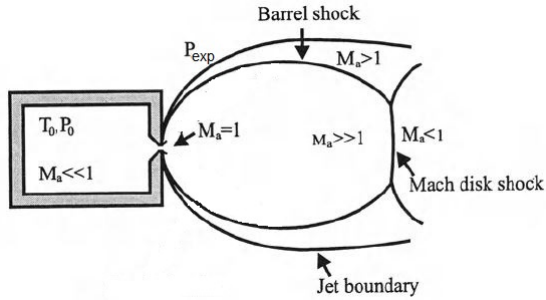


Figure 12: Schematic illustration of adiabatic expansion profile (adapted from Ref. [25]).

The velocity of the gas flow is described by a Mach number, M_a , that

is the ratio of the velocity of gas flow to the local speed of sound in the gas. In the nozzle container, the gas flow is subsonic ($M_a \ll 1$) and is characterized by stagnation temperature, T_0 and pressure, P_0 . The gas flow becomes sonic ($M_a = 1$) in the nozzle region as it accelerates toward the nozzle exit due to the pressure difference between P_0 and expansion chamber pressure, P_{exp} , ($P_0 > P_{exp}$). In the expansion region, the gas flow achieves supersonic speed ($M_a > 1$).

Adiabatic expansion leads to the temperature decrease in the gas. As a result of such cooling, the formation of clusters by condensation of the molecules is occurring. The most of the condensation occurs at the center of the expanding gas flow in a few nozzle diameter distances from the nozzle exit. During expansion, the sample molecules undergo many collisions with each other and the carrier gas. Molecules cool in the collision processes, losing most of their rotational and vibrational energy, and condensate. The carrier gas is used to cool the growing clusters and to carry off the heat of condensation, stabilizing clusters against dissociation. If the cooling is insufficient, the clusters are stabilized by losing some of the monomer subunits or by emitting photons.

Cooling efficiency in supersonic expansion can be enhanced by increasing the number of collisions (for example, by using smaller nozzle diameter). Stronger expansion generally leads to stronger cooling and better nucleation conditions. In the weak expansion, the cooling efficiency and nucleation conditions are worse.

It is assumed that cluster formation is based on three- and two-body collision processes [25]. Initially, three-body collisions dominate, so that by the collision of three separate molecules they nucleate into dimers (the heat of condensation of two molecules is carried away by the third molecule). When there are more clusters formed, two-body collisions of clusters with each other start dominating and result in cluster growth.

As the gas expands into the vacuum, the density decreases rapidly with increasing the distance from the nozzle. As a result, the number of collisions decreases and finally the cluster growth stops.

3.6 Data analysis

All data presented in this thesis was analyzed using Igor Pro 6.32A software with specifically-designed macros for peak fitting and work with PIY maps [26, 27].

The recorded ion TOF spectra were converted to the mass-to-charge ratio (m/z) scale according to $T = T_o + C\sqrt{m/z}$, where T_o and C are spectrometer's calibration constants that depend on spectrometer geometry and applied electric fields. The constants are easily obtained by solving the system of equations for two known mass peaks, for example, rest gas peaks

such as water and nitrogen.

The appearance energies, AE , of various ions were determined from the PIY plots in the ionization threshold region using following fitting function:

$$f(E) = \begin{cases} BG, & \text{if } E < AE \\ BG + k \times (E - AE), & \text{if } E \geq AE, \end{cases} \quad (14)$$

where E is the photon energy, k is the slope of rising edge of the PIY curve, and BG is a constant background level. The reported AEs are the intercepts of the two straight sections of the fitting function. The fitting function examples are shown in Figure 13 as blue lines for acetamide and protonated acetamide ion yield curves.

In the PIY experiment, the full dataset is represented by a 2-dimensional PIY map (photon energy vs. ion flight time) as shown in Figure 13 on the example of acetamide clusters. Two methods were used to extract the PIY curve (area of the specific ion peak in the TOF spectra vs. photon energy) from the map. In the case of well-isolated ion mass peaks, the area was obtained by integration and linear background removal, while in the case of overlapping peaks, the areas were obtained by least-squares curve fitting by Voigt profiles using the SPectral ANalysis by Curve Fitting (SPANCF) macro package [26, 27]. The ion yield curves obtained with the second method are shown in Figure 13 for acetamide monomer and protonated monomer.

In the case of cluster experiments, the spectra were normalized by measuring the drain current from the copper plate. The recorded photon flux was also corrected by the quantum efficiency function of copper plate signal. In the experiments with IL, the spectra were normalized by the silicon photodiode (AXUV-100, International Radiation Detectors, Inc.) current to account for the differences in the flux at the experimental chamber.

The photon energy in the PIY spectra was calibrated by measuring the PIY of argon gas and comparing the obtained ionization energy with a reference value of argon ionization energy (15.76 eV) [28].

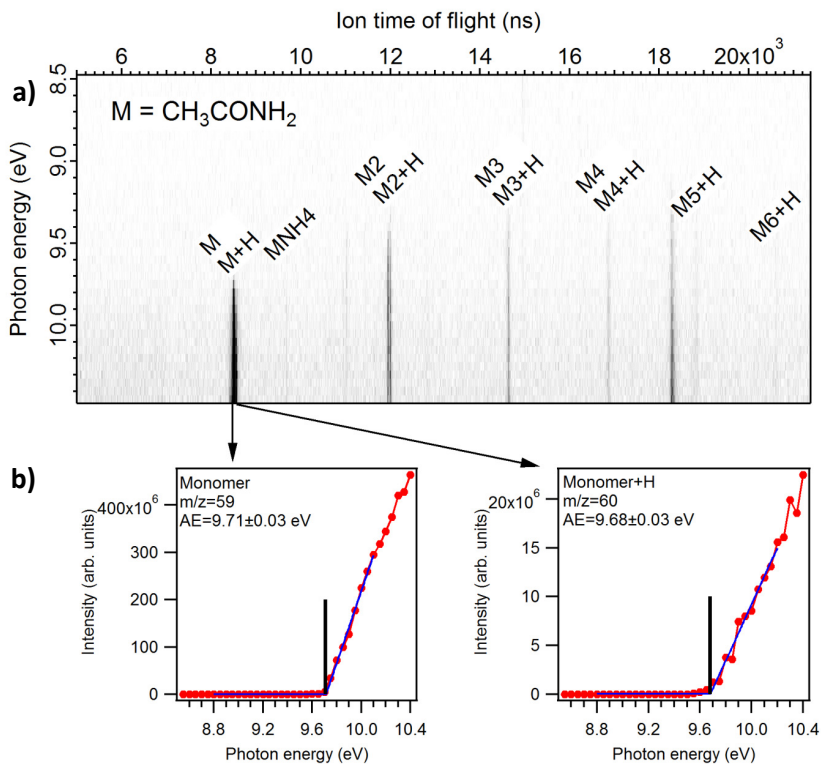


Figure 13: Panel (a) – partial ion yield map of acetamide clusters. Panel (b) – partial ion yield curves of acetamide monomer and protonated monomer extracted from the map. Blue lines represent the fit to the curves. The intersection point of the lines is marked with the vertical black line and represents the appearance energy (AE) of the ion.

4 Results and conclusions

4.1 Ionic liquids

Ionic liquids (ILs) are organic salts with a melting point close to or below the room temperature [29]. The first room-temperature IL, ethylammonium nitrate, was synthesized by Paul Walden in 1914 [29]. Later, ILs based on chloroaluminate anion were widely investigated but the applications were limited due to the high reactivity of the salts with water and oxygen [30]. In 1992, Wilkes and Zaworotko solved this problem by synthesizing air and water stable ILs based on imidazolium cation and tetrafluoroborate (BF_4^-) and hexafluorophosphate (PF_6^-) anions, making the field of ILs research highly popular from then on [31].

Due to their low vapor pressure, ILs were primarily used as a more environment-friendly alternative to the volatile organic solvents. However, ILs are finding new uses at a remarkable rate due to their extraordinary combination of physicochemical properties such as good ionic conductivity, chemical and thermal stability, liquid state, wide electrochemical window and unique solvating properties. New applications are being developed in various fields such as nanotechnology, electrochemistry, tribology, synthesis, catalysis, and materials science to name a few [32, 33].

During the PhD studies, the author has participated in several projects related to the applications of ILs in electrochemistry, material synthesis and tribology. For example, we investigated the electrochemical behavior of the Bi(111) and EMIm BF_4 /EMImBr mixture (EMIm is 1-ethyl-3-methylimidazolium cation) interface and concluded that IL mixtures used as an electrolyte are promising candidates for supercapacitors to achieve high energy densities [34]. By synthesizing the hybrid materials from the 1-methyl-3-[3-(triethoxysilyl)propyl]imidazolium chloride and titanium(IV) butoxide through aqueous sol-gel reaction, we immobilized the IL in the solid state, solving the problems related with leakage. From these highly homogeneous hybrid materials, we produced crack-free fibers and capillaries [35], conductive, hydrophobic, washing and thermally stable textile coatings functionalized with carbon nanotubes (CNT) [36], and well-dispersed hybrid nanoparticles [37]. Also, we developed new lubricant additives (nanoparticles mixed with phosphonium cation-based IL) to provide a significant enhancement in tribological performance of base oils already with a small amount of additive (1%) [38].

Nowadays, the most studied ILs typically consist of bulky polyatomic organic cations based on the derivatives of imidazolium, pyridinium, phosphonium, and ammonium. The anions could be of organic or inorganic origin and contain either one (*e.g.* halide ions) or more atoms (*e.g.* BF_4^- , PF_6^-). The counterparts of an IL can be easily modified, and

therefore a large number of potential ILs exists. IL modifications change drastically their properties such as melting point, reactivity, viscosity, solvation, miscibility, liquidus range, and conductivity. Therefore, it is not simple to find or customize an IL that would be perfect for a given task. Experimentally characterizing all possible ILs is unrealistic; thus theoretical calculations offer a more efficient way to characterize them. However, theoretical methods require experimental validation. Therefore, research on the fundamental physical chemistry of ILs is required.

The best way to experimentally study ILs, to make a comparison with theoretical methods, is to investigate them as single ion pairs in the gas-phase, *i.e.*, as overall neutral compounds consisting of one cation and one anion. The studies of IL vapor have begun by the breakthrough work of Earle *et al.* [39] who in 2006 demonstrated that some ILs could successfully be distilled at low-pressure conditions and moderate temperatures despite their ionic nature. However, no direct evidence about IL gas-phase nature were given at that time. Works of Leal *et al.* [40] along with Armstrong *et al.* [41] and Strasser *et al.* [42] were the first studies on the composition of the IL vapour phase that concluded that ILs evaporate as neutral ionic pairs (cation and anion linked together). Mass spectrometry and photoelectron spectroscopy are two methods that have mainly been used to investigate IL vapor phase. It was shown that IL vapor is neutral as no ions were detected in the absence of ionizing radiation. Also, it was demonstrated that ion pairs are easily subjected to fragmentation as, in general, the ionized parent molecule is not detected. The parent molecule was experimentally detected when soft ionization methods such as electric field ionization (10-20 V/nm) were used [43]. The example molecules for such studies are the imidazolium-based ILs that contain a bis[(trifluoromethane)sulfonyl]imide (Tf_2N^-) anion. These ILs were shown to be thermally stable. It was found that by fluorinating the anion, thermal stability improves. Chemically less reactive large anions exhibit enhanced thermal stability. We studied an imidazolium-based IL with BF_4^- anion as this type of ILs is very common, commercially available and tested in many applications due to their large electrochemical window, relatively low viscosity, and high conductivity. However, the mass and electron spectroscopic data on ILs with BF_4^- anion is limited.

Papers I and II of the thesis present experimental results of the valence photoionization of gas-phase EMImBF₄ studied by time-of-flight (TOF) mass spectrometry and photoelectron spectroscopy, respectively. In mass spectrometry study, photon-energy-dependent TOF spectra were measured to decipher the energetics of the fragmentation pathways of the IL. In the case of multiple possible assignments of a certain peak, the most likely fragmentation product was identified computationally. Calculations were performed using Spartan 14 software [44] with B3LYP functional

and 6-31G** basis set. Calculated activation energies were determined by the energy difference between the parent molecule and the resulting fragment. Thus, the calculation estimates the minimum energy required for the fragmentation, while the appearance energy (AE) of the fragment might be higher due to transition state energy barriers. The AEs were determined by analyzing the TOF spectra measured at different photon energies and selecting the AE as the energy at which the signal starts to appear. In Paper I, the PIY curve of the complex of peaks at m/z 110, 111, 112 is presented, but in this work, the PIY curve of a single ion EMIm^+ at m/z 111 is shown.

In the photoelectron spectroscopy study, the comparison of experimental electron spectrum and calculated density of states (DOS) using DFT and MP2 methods was performed, which allowed us to draw conclusions on the electronic structure of EMImBF_4 and the subject of electron relaxation.

4.1.1 Mass spectrum of EMImBF_4 : Observed fragments

Figure 14 depicts two mass spectra of EMImBF_4 vapor that were measured at different temperatures at 20 eV photon energy. Let us first describe the

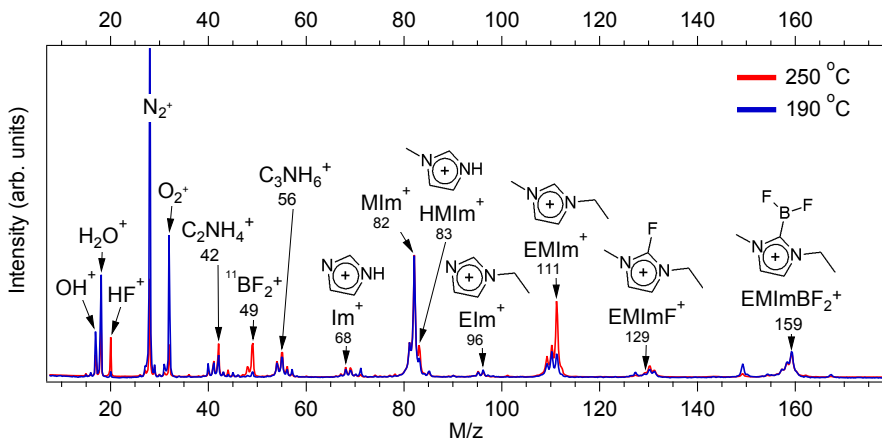


Figure 14: Mass spectra of EMImBF_4 vapor measured at 20 eV photon energy at liquid cell temperatures 190 °C (blue) and 250 °C (red). Spectra are normalized to m/z 82.

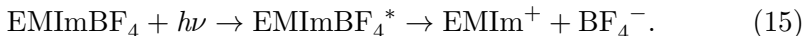
observed fragments and then proceed to the discussion of their possible formation channels.

The signal of background gases (O_2^+ , N_2^+ , H_2O^+ , OH^+) is quite high due to low vapor pressure of IL. The contaminants desorbed from the walls of the spectrometer were present at m/z of 43-46, 57, 71, 85, 127, 149,

154, 167. The most anticipated fragment is an intact cation EMIm^+ at m/z 111, the presence of which shows that IL evaporation as ion pairs is occurring. Also, peaks that were one and two mass units lower were detected and assigned to be dehydrogenated and doubly dehydrogenated EMIm^+ , correspondingly. The dominant peak at m/z 82 corresponds to the MIm^+ ion that represents an intact cation that has lost its ethyl group. Also, dehydrogenated and protonated MIm^+ ions were present at m/z 81 and 83, respectively. By the loss of methyl group from the intact cation, EIm^+ ion at m/z 96 is formed. The intact cation that has lost both of its alkyl chains leaving behind one H atom produces a fragment Im^+ at m/z 68. Fragments at m/z 41, 42 and m/z 54, 55, 56 are most likely the products of the intact cation fragmentation due to double bond breaking of the ring and represent the ions C_2NH_3^+ , C_2NH_4^+ and C_3NH_4^+ , C_3NH_5^+ , C_3NH_6^+ , correspondingly. The fragments that were heavier than the intact cation were also detected at m/z 129 and 159. We assigned them to be dehydrogenated EMImF^+ and dehydrogenated EMImBF_2^+ cations. However, these peaks came in an ensemble with m/z 130, 131 and m/z 157, 158, respectively. The peaks at m/z 20 and 49, detected at higher temperatures, are HF^+ and $^{11}\text{BF}_2^+$ ions, respectively.

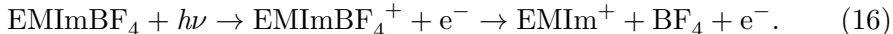
4.1.2 Possible photofragmentation pathways of EMImBF_4

Two mechanisms following the photoabsorption were identified for intact cation (EMIm^+) formation. The first one is photoexcitation of a neutral parent molecule followed by dissociation of a neutral excited state into cation and anion. We calculated that the activation energy of 4.2 eV is required for this reaction:



Although the activation energy is smaller than the calculated first excited state energy (6.7 eV), this process is not possible before photoabsorption takes place. The fragmentation should be possible as soon as the excitation to the LUMO level occurs. Therefore, EMImBF_4 is unstable following photoabsorption and easily fragments after excitation.

The second mechanism for production of EMIm^+ cations following photabsorption is photoionization that results in dissociation of the parent molecular cation into the intact cation and neutral BF_4 :

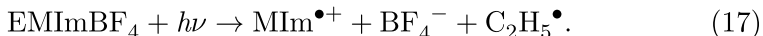


This pathway has a higher activation energy of 10.7 eV. From our experiment, we could not determine the branching ratio between these two fragmentation channels. However, Koh and Leone reported a surprising

branching ratio of 0.18:0.82 in the photon energy range of 17-26 eV for $\text{EMImTf}_2\text{N}^-$ dissociation with the emission of the electron and without, correspondingly [45]. Using velocity map ion imaging technique, they observed EMIm^+ cations with zero kinetic energy (all energy is carried away by photoelectron), and fast cations and fast anions (the photon energy is transferred to the fragments, no electron emission). In addition, an UV study of $\text{EMImTf}_2\text{N}^-$ at 5.5 eV photon energy identified another dissociation channel via charge transfer to form radical species EMIm^\bullet and $\text{Tf}_2\text{N}^\bullet$ upon dissociation [46]. We cannot comment on that as in our experiment neutral species could not be seen.

The EMIm^+ cation has a double-sloped PIY curve as shown in Figure 15. By applying the fitting function (Equation 14) to the first slope, the appearance energy (AE) of EMIm^+ was determined to be 7.71 ± 0.10 eV. To the second slope a linear fit was applied and by extrapolation of the fitted line to the x-axis, the energy at which the yield of ions starts to significantly increase for the second time was determined to be 9.31 ± 0.10 eV. The appearance energy of EMIm^+ corresponds roughly to the calculated LUMO-HOMO difference of EMImBF_4 (6.9 eV by B3LYP and 7.5 by MO6 functional). Excited state calculation predicts the first significant dipole-allowed excited state at 7.6 eV and the next ones at 9.5-10.1 eV that is in good agreement with the experimentally determined energies from the PIY curve. Therefore, we explain the nature of the double-sloped PIY curve by two strong dipole transitions to excited states of IL that are separated in energy. The ion yield is much higher at higher energy. The calculated absorption cross section is also many times larger (by a factor of 6-10) than in the case of the AE. However, the fragmentation rates and pathways may also differ significantly. Near the AE, dissociation of the ion pair into radicals may occur [46]. Therefore, most of the EMIm^+ signal will be lost for the detector. At the second energy (9.31 ± 0.10 eV), the dissociation to cation and anion with and without electron emission may dominate increasing the EMIm^+ signal.

The MIm^+ cation at m/z 82, that is the strongest peak in the spectrum, might be formed as a result of dissociation of neutral excited parent molecule by the loss of the ethyl group from the EMIm^+ according to the following reaction with the calculated activation energy of 8.1 eV:



This is in good agreement with experimental appearance energy (AE) AE = 8.2 eV.

The reaction pathway for HIm^+ ion at m/z 83 has a lower activation

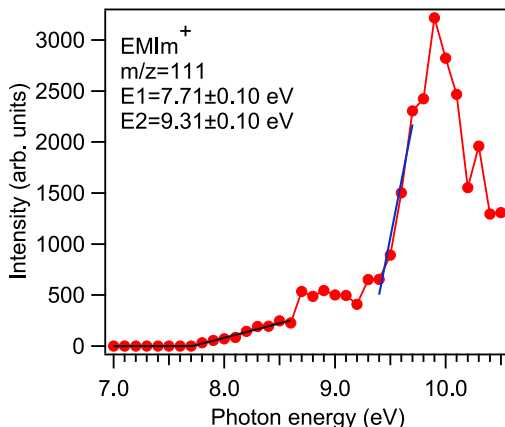
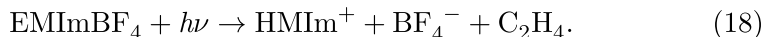


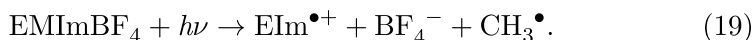
Figure 15: Partial ion yield curve of EMIm^+ ion measured at temperature of 230°C . The curve was obtained by plotting the areas of the peak in TOF spectra taken at different photon energies in the range of 7-10.5 eV with a 0.05 eV step.

energy value, 5.5 eV,:

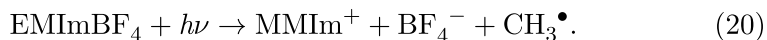


The $\text{AE} = 7.8 \text{ eV}$ for HIm^+ .

The small signal at m/z 96 could represent EIm^+ and/or dehydrogenated MMIm^+ ions. In the first case, the ion is formed by the loss of a methyl group from EMIm^+ :



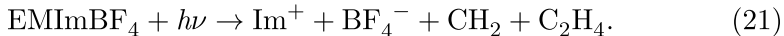
In the second case, EMIm^+ cation loses a methyl group from the ethyl side chain to form dehydrogenated MMIm^+ :



However, the activation energy calculation showed that the production of EIm^+ ions requires less energy (8.6 vs 9.3 eV), therefore making this ion the likely ion contributing to the signal. The $\text{AE} = 8.3 \text{ eV}$ for this ion.

The signals detected at m/z 68, 69 might be the secondary fragmentation products of EMIm^+ formed by the loss of both alkyl side chains from the imidazolium ring accompanied by the hydrogen migration from the separating alkyl group to the imidazolium ring. For an ion at m/z 69 two hydrogens (one from ethyl, another from methyl group)

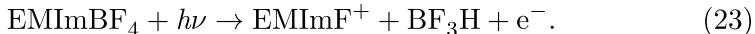
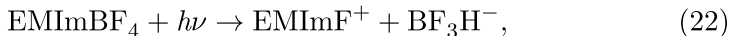
migrate to the imidazolium ring:



The activation energy for the above reaction is 10.6 eV, while for the formation of an ion at m/z 68 it is 10.1 eV. However, experimental AE for fragment at m/z 68 were higher than 10.5 eV. There might be a barrier for hydrogen migration that our calculation does not consider.

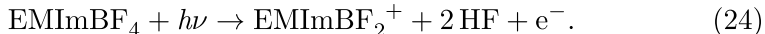
EIm^+ and Im^+ peaks have roughly the same intensity, and are much weaker than MIm^+ peak. Therefore, the loss of ethyl group seems to be more favorable than the loss of the methyl group or the loss of both alkyl side groups.

The fragments with the mass higher than the EMIm^+ cation were detected as well and were assigned to be the dehydrogenated EMImF^+ and dehydrogenated EMImBF_2^+ (see the structures in Figure 14). There are two possible fragmentation pathways for dehydrogenated EMImF^+ with activation energies of 7.0 and 10.3 eV, respectively:



The experimental AE of dehydrogenated EMImF^+ is about 9.8 eV. However, these fragmentation pathways cannot explain the peaks at m/z 130 and 131, which may originate from the hydrogenated parent molecule. The presence of the hydrogenated EMIm^+ was observed at m/z 112.

Doubly dehydrogenated EMImBF_2^+ cation with ^{11}B isotope at m/z 158 and ^{10}B isotope at m/z 157 can form via following reaction (act. en. 10.8 eV):



However, this reaction does not explain the strongest peak at m/z 159, which also may originate from the hydrogenated parent molecule.

To sum up, the AEs for EMImBF_4 were experimentally determined by PIY technique and explained by DFT calculations. Overall, there is a good agreement between the experiment and theory. EMImBF_4 was shown to fragment into intact cation and anion below the ionization threshold after photoabsorption as a result of dissociative excitation. Computationally, the double-slope nature of the EMIm^+ PIY curve was explained by two groups of dipole-allowed excited states that are separated in energy and excitation to which leads to the fragmentation of the neutral excited molecule via separation of the cation and the anion.

4.1.3 Thermal degradation

As indicated by Figure 14, no major effect on the temperature was detected in the mass spectrum of EMImBF₄. With the increase of the temperature, all signals increased, but the structure of the spectrum remained the same. However, the relative intensity of three signals at m/z 20, 49, and 111 increased noticeably. Here, we will discuss the possible thermal degradation mechanisms that can contribute to the peaks at m/z 20 and 49, although it is still unknown why the production of intact cations at m/z 111 increased more at higher temperatures in comparison to other sample-related peaks.

Thermal stability is a critical parameter for many applications of ILs. Thermal stability of ILs depends on the type of the cation and anion and their modifications (*e.g.* side chain length of the cation, functionalization) [47]. However, it is often claimed that the anion plays a major role in determining the thermal stability of an IL as the decomposition temperature may change from 200 to 400 °C by varying the anion type [47]. Generally, the thermal stability of ILs increases with decreasing the nucleophilicity of the anion. It was found that by fluorinating the anion, thermal stability improves making ILs with the anions such as BF₄⁻, PF₆⁻, and Tf₂N⁻ more thermally stable, while ILs with halide anions are the least stable.

The decomposition onset temperature of EMImBF₄ was reported to be 413 °C [47], well above the temperatures used in this work. Ohtani *et al.* investigated the thermal degradation of EMImBF₄ under pyrolytic conditions [48]. Upon decomposition, EMImBF₄ was shown to form 1-alkylimidazoles. They may be formed through bimolecular nucleophilic substitution (S_N2 mechanism), which proceeds through nucleophilic attack of fluoride, or simple thermal cleavage of the C-N bond. In addition to 1-ethylimidazole (m/z 96) and 1-methylimidazole (m/z 82), the formation of ethylene (m/z 28), fluoromethane (m/z 34), fluoroethane (m/z 48) and HF (m/z 20) was observed. Noteworthy, no boron-containing products were detected [48].

In our experiment, no fluoroalkanes were observed at the highest temperature used (see Figure 14). The peak at m/z 28 represents most likely the rest gas N₂⁺, not the ethylene as its signal decreased at the higher temperature. The presence of 1-alkylimidazoles, however, cannot be easily eliminated as there are signals at m/z 82 and 96 in the mass spectrum. IL photodissociation and degradation can both contribute to the signals. Noteworthy, under pyrolytic conditions, different 1-alkylimidazoles were of equal intensity, while in our mass spectrum, the intensities of the peaks at m/z 82 and 96 differ significantly.

HF⁺ ion, which intensity increases from negligible value at 190 °C to significant value at 250 °C, might be a product of IL degradation. Multiple

sources for HF^+ formation are possible. The first one is the hydrolysis of the anion in the presence of water [49]. In our experiment, this is unlikely since the IL was purified under vacuum overnight to get rid of water traces. The second option is the formation of dehydrogenated EMImBF₃ in the liquid phase with a release of HF [50]. This could give a second explanation for the peak at m/z 159 that could form due to the photofragmentation of EMImBF₃ by the elimination of fluorine. The third possibility for HF formation is the IL decomposition through the formation of the carbene (1-ethyl-3-methylimidazolium-2-ylidene) via elimination of neutral HF and BF₃ [51]. The carbenes were shown to form in ILs that have an anion with increased basicity such as acetate [52]. The carbene would be at m/z 110, while BF₃⁺ would then overlap with Im⁺ signal at m/z 68. BF₃ can dissociate by losing one fluorine atom to give an ion $^{11}\text{BF}_2^+$ at m/z 49. As HF^+ , the $^{11}\text{BF}_2^+$ signal depends highly on the temperature.

In conclusion, thermal decomposition signs were observed in the mass spectrum of EMImBF₄ vapor at temperature of 250 °C in the form of HF^+ and BF_2^+ ions. However, they were not major enough to affect our conclusions on the fragmentation pathways. Thermal degradation mechanism for HF release might be the formation of the carbene by abstraction of the acidic proton from the cation by fluorine atom of the anion and elimination of BF₃. Then, BF_2^+ ion could be formed by BF₃ photodissociation. Therefore, a mixture of IL vapor and its decomposition products is detected at elevated temperatures. The understanding of possible degradation mechanisms can help differentiate between the signals coming from the photofragmentation of IL and ionization and fragmentation of decomposition products.

4.1.4 Electronic structure of EMImBF₄

The valence electronic structure of ILs is important for the understanding of the interactions between the cationic and anionic components of ILs to answer the question how the electronic structures of the cations and the anions combine to form the overall electronic structure of the IL.

We investigated the valence electronic structure of EMImBF₄ (see Figure 16) IL in the gas phase by photoelectron spectroscopy in the VUV region with synchrotron radiation at I411 beamline of the former MAX-II storage ring. In the experiment, IL was evaporated from a quartz crucible (liquid phase at 190 °C) to the ionization region, where the vapors interacted with the radiation of 60.6 eV photon energy and the beam diameter of 1 mm. Pass energy of the electron analyzer was chosen to be 100 eV.

The valence photoelectron spectrum was compared to the calculated spectra obtained using DFT (B3LYP hybrid functional) and MP2 methods

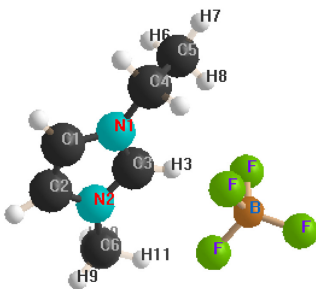


Figure 16: Structure of EMImBF₄ with numerated atoms of the cation.

(see Figure 17 and Figure 18, correspondingly). The calculations were performed using Spartan 14 software [44] and Gaussian basis sets 6-311G^{**}. The density of states (DOS) spectra were obtained by convolution of the calculated discrete states with a Gaussian function under the assumption that the electron emission intensities are the same for each orbital and the photoemission process is much faster than the rearrangement of the electron system after the absorption of the photon (the sudden approximation). To fit the calculated spectra to the experimental one, the energy scale of the DOS spectra was contracted (scaling factor of 1.1) and shifted to 2 eV and -3.7 eV for DFT and MP2, correspondingly.

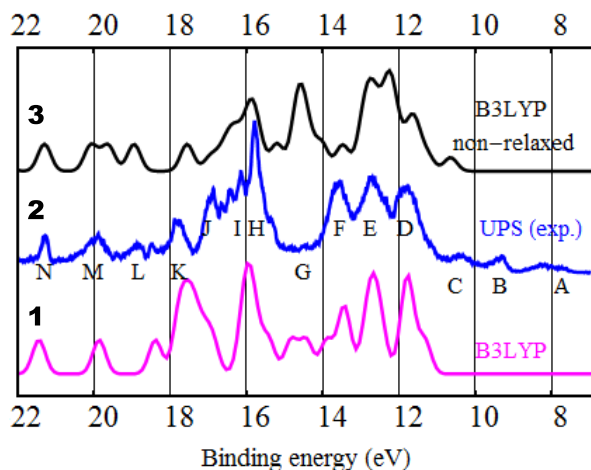


Figure 17: The experimental electron spectrum of EMImBF₄ vapor (2) compared to DFT calculated valence density of states for neutral molecule (1) and for ionized molecule (3). For peak assignments see Table 1.

Let us first explain the assignments used in Figure 17 and Figure 18. The notation "UPS (exp.)" is used for the experimental spectrum

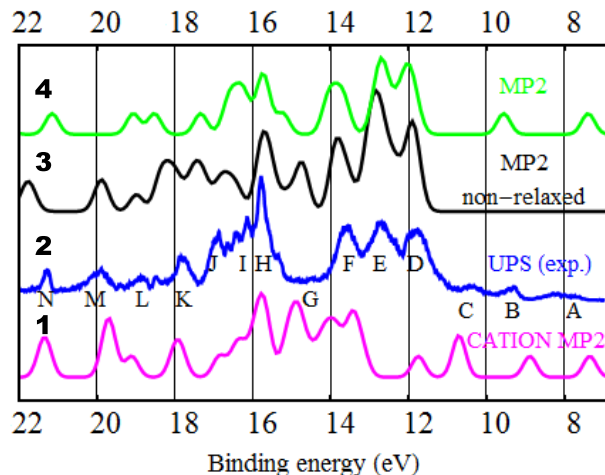


Figure 18: The experimental electron spectrum of EMImBF₄ vapor (2) compared to MP2 valence density of states calculation for neutral molecule (4), ionized molecule (3), and neutral structure of IL's cation – 1-ethyl-3-methyl-1H-imidazole radical (1). For peak assignments see Table 1.

of EMImBF₄ vapor. "B3LYP non-relaxed" and "MP2 non-relaxed" calculations refer to the calculation of positively charged EMImBF₄ in the geometry of the neutral molecule (will be referred to as ionized molecule). The calculations are non-relaxed in terms of nuclear motion but relaxed in terms of electronic configuration. Notations "MP2" and "DFT" refer to the EMImBF₄ neutral molecules with optimized geometries calculated using the corresponding method. The MP2 calculation denoted as "CATION MP2" was made for the neutral structure of IL's cation – 1-ethyl-3-methyl-1H-imidazole radical.

In the experimental spectrum (spectrum 2 in Figure 17 and Figure 18), the peaks are marked with letters, the assignments of the peaks are presented in Table 1. These are tentative assignments since calculation showed that many valence states of the EMImBF₄ are delocalized over the full molecule, making it difficult to assign the strongest contributing atom. Two major peak complexes are seen in the experimental spectrum: one at around 11-14 eV binding energies (peaks D-E) and another at 15-18 eV (peaks H-J). They are separated by a gap. Further on in the text, the region to the right side of the gap will be referred to as outer valence states and region to the left side as inner valence states, correspondingly.

The cross section of photoemission is much larger in case of F 2p orbitals compared to the 2p orbitals of carbon and nitrogen that are the constituents of the cation [53]. Therefore, the anion BF₄⁻ has a larger

Table 1: Tentative assignments of the peaks detected in the experimental electron spectrum of EMImBF₄ vapor.

Peak	E_{bin} (eV)	Contributing atoms and character
A1 A2	7.8 8.2	C1-C3, N1, N2 (π -bonds)
B C	9.4 10.4	
D	11.8	Mostly F 2p (except the shoulder on the right which is C 2p)
E F	12.8 13.6	Mostly F 2p
G1 G2	14.4 14.8	
H	15.8	F, B, C3, C6, N1 (anion and cation atoms)
I	16.2	C3, H3, C1, C2, N1, N2
J	16.9	Mostly C 2s (σ -bonds)
K	17.8	C1-C3, C6, N1, N2 (π -bonds)
L M N	18.8 19.8 21.4	C 2s (σ -bonds)

spectral contribution, intensity-wise. The outer valence states are mostly derived from the anion’s F 2p orbitals (peaks D, E, F). However, the top of the valence states (low-intensity peaks A, B, C) has a cationic character (see Table 1). The inner valence states (peaks H-N), as the comparison to "CATION MP2" calculation shows (see Figure 18, spectrum 1), have mostly cationic origin.

The outer valence states are represented quite well by DFT calculation of the neutral EMImBF₄ (spectrum 1 in Figure 17). If the removal of a charge is taken into account, DFT represents very well also the inner valence states (spectrum 3) and MP2 calculation – the outer valence states (Figure 18, spectrum 3). The peaks A, B, and C, that have the cationic origin, are not represented by either of the DFT calculations, while MP2 calculation of neutral molecule succeeds to represent two of the peaks. The low-intensity peaks detected in the gap region and marked as G are coming from the alkyl groups of the cation. DFT calculation predicts two states around that binding energy, while MP2 calculation shows a small gap. The low cross sections of the hydrogen atoms and the s-symmetry orbitals explain their weak signal in the experimental spectrum.

One important result of this study was the observation of electron relaxation. This phenomenon shows the importance of including electron correlation into calculations for this class of compounds. By comparing the outer and inner valence states of the experimental spectrum to the

calculated ones for neutral and ionized molecules, it was possible to make conclusions whether the electronic relaxation is occurring at the corresponding region. According to Figure 17, the inner valence states' DOS of ionized molecule is in a better agreement with the experiment than the DOS of neutral molecule. Therefore, a conclusion can be drawn – when the electron is removed from the inner valence states, complete relaxation of the electronic structure is occurring. In the case of outer valence states, the DOS spectrum of neutral molecule reflects better the experimental result, indicating that little or no relaxation is occurring in this region. The MP2 calculation (Figure 18) predicts either too much relaxation or incomplete relaxation in the inner valence states as the peaks I, J, K, and N seem to shift to higher binding energies (electrons move closer to the nucleus), while the peaks L and M agree well with the experiment. The charge distribution calculation by MP2 showed that the negative charge is preferably removed from the cation (atoms of imidazolium ring), while DFT predicted the negative charge to be removed from both anion and cation. Therefore, in the case of MP2, the strong electronic relaxation is expected in the inner valence states, while DFT predicts relaxation in both inner and outer valence states. MP2 prediction is in a better agreement with the experimental result, since "non relaxed MP2" correctly predicts no significant relaxation for the D–F peaks of anion origin. However, cation-related peaks A and B disappear in the non-relaxed calculation. Thus, it can be concluded that there is no significant relaxation in the anion and the outer valence states of the cation.

There is an overall qualitative agreement between the experiment and the calculated DOS. However, it seems to be difficult to describe the shape of inner and outer valence states with one type of calculation. The best agreement with the experiment shows MP2 calculation. Despite the fact that it overestimates the relaxation in the inner valence states, has discrepancies in the binding energies of the L, K, and F peaks and does not describe the C peak. Contrary to DFT, the MP2 calculation shows the topmost outer valence peaks and describes the HOMO level correctly.

In conclusion, the comparison of the experimental spectrum and calculated density of states using MP2 and DFT methods was performed. The MP2 method was found to describe the experiment more accurately. Strong relaxation of the electronic structure was shown to be occurring in the inner valence states of the cation, while no significant relaxation in the anion and the outer valence states of the cation was observed. Contrary to regular salts such as NaCl, where the top of the occupied states is derived from the anion, in EMImBF₄, it is derived from the cation.

4.2 Clusters

A cluster is an aggregate of particles (atoms or molecules) that is too small to be thought of as a bulk material and too large to be considered as a single molecule. The cluster could contain from a few to several thousand units, called monomers. The common phrase in cluster research is that they "bridge the gap between single atoms or molecules and solids". This intermediate state of matter possesses a unique set of physicochemical properties different from those of bulk and single molecules.

The cluster research is very extensive as clusters might be formed from any element of the periodic table, even from rare gases. Also, considering the facts that their physicochemical properties change depending on their size, that a cluster of a given size might take on a variety of geometrical structures, that they might be homogeneous (one type of particles) or heterogeneous (a mixture of different particles) and might be held together by different forces, the clusters represent almost endless resources of new materials. Therefore, clusters have a vast number of possible applications in electronics, biomedicine, and materials science among others [54].

In this work, the focus is on gas-phase molecular clusters held together by hydrogen bonds. Two cluster systems were studied: acetamide and acetic acid clusters. The molecules of acetamide, CH_3CONH_2 , and acetic acid, CH_3COOH , are structurally similar. They differentiate by one functional group: in acetamide, $-\text{OH}$ is substituted by $-\text{NH}_2$.

The molecules of acetamide and acetic acid were found in space and therefore are of biological interest as prebiotic molecules [55, 56]. Acetamide is the largest molecule detected in space that contains a peptide group ($\text{CO}-\text{NH}-$), while acetic acid is not too different from the simplest amino acid, glycine, $\text{NH}_2\text{CH}_2\text{COOH}$. Therefore, both of the molecules could be the source for larger peptides (fundamental components of cells).

By condensation of molecules into clusters, we obtain a simple model system to study biologically important chemical processes triggered by the VUV radiation (*e.g.* ionization, proton transfer, radiation damage and radical release). In clusters, initial and final structures can be relatively easily specified, while experimental studies of bulk systems tend to mask the details of reaction mechanisms due to the influence of the environment. For example, photoionization of small acetamide and acetic acid clusters (especially their dimers) makes it possible to probe the consequent dynamics along the $\text{C}-\text{H}\cdots\text{O}=\text{C}$, $\text{O}-\text{H}\cdots\text{O}=\text{C}$ and $\text{N}-\text{H}\cdots\text{O}=\text{C}$ types of hydrogen bonds in their most basic form, excluding any additional influence of the environment. Currently, investigations of biomolecular clusters structure and properties is an attractive growing field of research where theory [57] and experiment [58] go hand in hand.

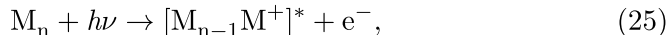
Papers III and IV of the thesis present experimental results of valence

photoionization and the consequent fragmentation of gas-phase acetamide and acetic acid clusters by time-of-flight mass spectrometry, mostly focusing on the dimers. Paper III investigates the photofragmentation of acetamide clusters, making use of partly deuterated acetamide to elucidate the source of the proton in proton transfer reactions following the photoionization. Paper IV addresses the clustering condition-dependent fragmentation of acetic acid clusters, presents the appearance energies of the fragments for both compounds and compares the observed fragmentation pathways, providing computational support for both samples.

The goal of the calculations was to determine the geometries and energies of the ionized dimers and to calculate the energy barriers to the conversion of the structures formed from vertical ionization to the lowest energy geometries. Therefore, intramolecular hydrogen migration processes in both dimers and dissociative NH_3^+ ion migration in acetamide dimer were probed. Calculations were performed with GAMESS software [59] using the restricted open-shell Hartree-Fock method at the MP2/6-311++G** level of theory. The transition state (TS) and thus the energy barrier of the hydrogen transfer from methyl group within one monomer subunit in an ionized dimer was found by performing TS calculations. The intrinsic reaction coordinate calculation was performed to confirm that the TS indeed represents the desired reaction.

4.2.1 Photofragmentation pathways

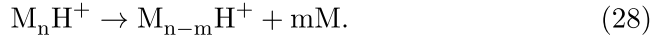
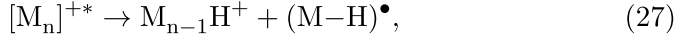
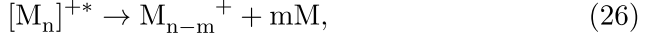
The molecular clusters, held together by weak hydrogen bonds, tend to easily fragment after photoionization. There is an important difference between ILs and molecular clusters. In IL, two subunits are anion and cation in a neutral molecule, but in clusters, all subunits have equal charge. Therefore, no charge separation following neutral photoexcitation is expected to occur in molecular clusters, contrary to ILs. In principle, clusters could fragment after photoexcitation, but the products will be neutral and therefore not detected. Photoionization of hydrogen-bonded molecular clusters proceeds through ionization of a single monomer subunit within the cluster, accompanied with electronic and vibrational excitation [54]:



where M is the monomer and $n \geq 2$ is a number of monomers in a cluster. Therefore, ionized clusters are initially in an unstable geometry, but can stabilize through configurational changes within or across monomer subunits.

Some relaxation mechanisms are characteristic for all hydrogen-bonded cluster systems composed of polar molecules and therefore could be generalized. Such mechanisms include the loss of the intact monomers

from a cluster, dissociative proton transfer from the ionized monomer subunit to the neutral one, and the loss of intact monomers from the protonated clusters in the case of excessive energy deposited on the clusters, according to the following equations, correspondingly:



The processes of monomer extraction were not directly studied in this work but were observed for protonated acetamide clusters by examining the size distributions of protonated cluster ions at increasing photon energies. Figure 19 demonstrates how an increase in the photon energy shifts the cluster ion distribution towards smaller sizes, implying that the large protonated clusters start to dissociate more by losing some amount of monomers to produce smaller protonated clusters.

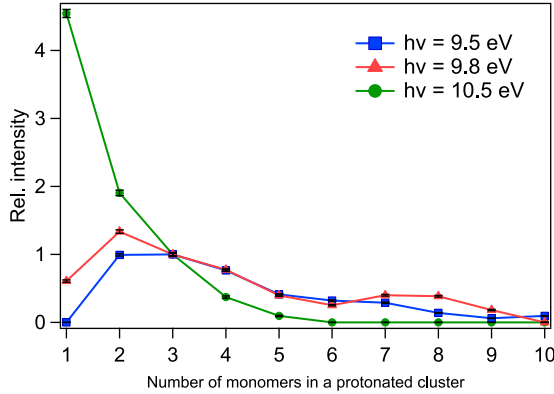
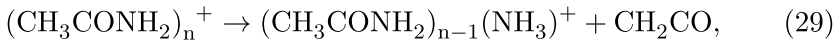
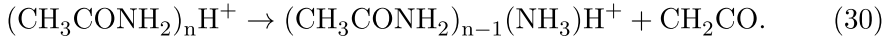


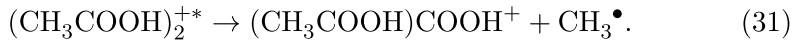
Figure 19: Distribution of protonated acetamide cluster ions at 9.5 eV, 9.8 eV, and 10.5 eV excitation energies, normalized to $(CH_3CONH_2)_3H^+$.

Some relaxation mechanisms are specific for each cluster system and directly depend on the structure of the intact monomers. For example, in acetamide clusters, the C-N bond breakage was observed that resulted in the production of ammoniated clusters from neat and protonated clusters, correspondingly:





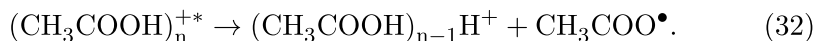
In acetic acid clusters, the characteristic fragmentation pathway was the breakage of C-C bond detected only for the dimers:



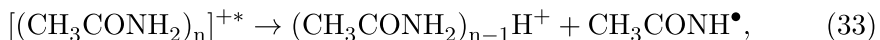
In conclusion, the main fragmentation channels identified for studied clusters are breaking of hydrogen bonds followed by extraction of monomer subunit(s), proton transfer reactions followed by dissociation, C-C bond breakage characteristic for acetic acid dimer, and C-N bond breaking followed by NH_3^+ transfer in acetamide clusters. In the next sections, proton and NH_3^+ ion transfer mechanisms will be discussed in more detail.

4.2.2 Proton transfer reactions

Protonated fragments dominate the mass spectrum of the studied clusters. Protonated clusters up to tetramers were detected for acetic acid in the form of $(\text{CH}_3\text{COOH})_n\text{H}^+$ and up to hexamers for acetamide in the form of $(\text{CH}_3\text{CONH}_2)_n\text{H}^+$. The main creation mechanism for these ions is the fragmentation of larger clusters by separation of fragments, which is accompanied by fast proton transfer reaction from the primarily ionized molecule to its neutral partner via hydrogen bond. Thus, the orientation and configuration of the cluster systems prior to proton transfer are critical factors that influence the conclusions on the exact proton transfer path. The easiest way to identify the exact proton transfer path in clusters is to consider the configuration of the dimers as they have fewer options of possible subunit arrangements. For example, for acetic acid dimer, the geometry is known to be cyclic with two H-bonds between the hydroxyl group and carbonyl oxygen [60, 61, 62]. Thus, the proton transfer occurs from the hydroxyl group [63, 64, 65]:



In Figure 20, three possible arrangements of acetamide dimer are presented with a schematic representation of proton transfer mechanisms showing that there are two proton sources: amino and methyl groups. Both proton transfer mechanisms produce the protonated ions with the same chemical formula, but different tautomers of deprotonated acetamide radicals:



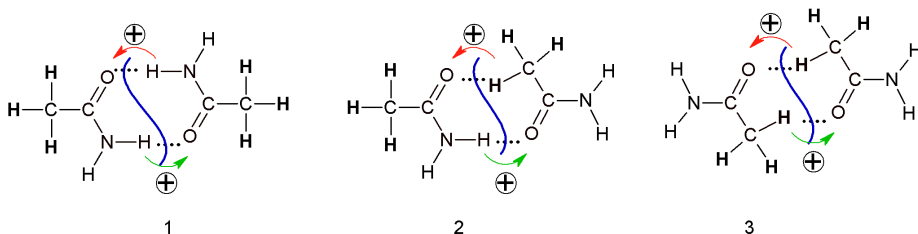
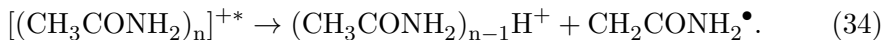


Figure 20: Schematics of proton transfer mechanism shown on differently arranged acetamide dimers. Blue lines are the borders across which the proton transfer occurs before separation of the fragments. Depending whether the subunit on the left or right becomes ionized, the proton transfer follows a green or a red arrow, correspondingly.

To track the dominant proton transfer path and therefore elucidate the most stable structure of acetamide dimer in the gas phase, a comparative experiment with partly deuterated acetamide (CD_3CONH_2) was carried out. It was shown that normal and deuterated acetamide clusters generally fragment in the same way by comparing their mass spectra (see Paper III). In the experiment with the partially deuterated sample, the products of the dimer fragmentation reaction could be easily differentiated. If the deuteron transfer occurs from the methyl group, the signal at m/z 64 appears; if the proton transfer occurs from the amino group, the signal at m/z 63 appears. The region of interest in the mass spectrum of the deuterated acetamide clusters is shown in Figure 21 with both signals detected. Comparing the intensities of the peaks, it is evident that the most likely proton source is the amino group as the proton transfer from the amino group occurs in 86% of cases, while deuteron transfer from the methyl group only in 14% of cases.

The signal at m/z 61 might originate from the monomer dissociation by the loss of hydrogen or it might be the dimer dissociation product. If after proton transfer in the dimer, the charge is localized on a fragment with fewer hydrogens, the signal at m/z 61 could arise. If this signal indeed arises from the dimer fragmentation, it only supports our finding that the proton transfer is facilitated by the amino group. In another scenario, if the methyl group would be responsible for deuteron transfer, a peak at m/z 60 that corresponds to $(\text{M-D})^+$ would also be expected. Since the signal at m/z 60 is missing, a conclusion can be drawn that the amino group is

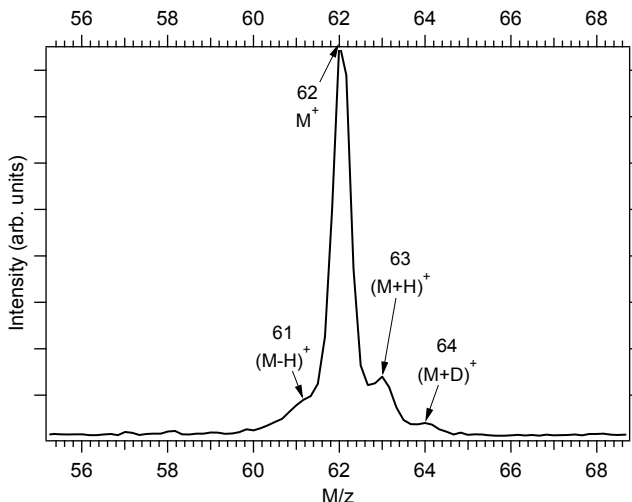


Figure 21: Mass spectrum of partly deuterated acetamide clusters $(\text{CD}_3\text{CONH}_2)_n$ near the monomer (M) region measured with Ar gas discharge lamp at 11.62 eV.

the dominant source for protons in proton transfer reactions independent whether the charge localizes on a fragment with more or less hydrogens.

Based on the above-discussed finding, the structural arrangements of the acetamide dimers with the $\text{N}-\text{H}\cdots\text{O}=\text{C}$ bonds are more common than with the $\text{C}-\text{H}\cdots\text{O}=\text{C}$ bonds. Thus, the structure 1 in Figure 20 with two $\text{N}-\text{H}\cdots\text{O}=\text{C}$ H-bonds is the most stable one. The structure 2 with one $\text{C}-\text{H}\cdots\text{O}=\text{C}$ and one $\text{N}-\text{H}\cdots\text{O}=\text{C}$ H-bond is less stable, while structure 3 with two $\text{C}-\text{H}\cdots\text{O}=\text{C}$ bonds is the most unstable. This result is in agreement with Albrecht *et al.* infrared spectroscopy study [66] who also identified the most stable geometry of acetamide dimer to be cyclic and connected through amino group hydrogens.

To sum up, in acetamide clusters, two proton transfer mechanisms are possible following the photoionization: from amino and methyl groups. The amino group, however, is the dominant source of protons. The analysis of different monomer subunit arrangements in the dimer in terms of proton transfer showed that the most stable structure of the acetamide dimer in the gas phase is cyclic with two $\text{N}-\text{H}\cdots\text{O}=\text{C}$ hydrogen bonds.

4.2.3 Formation of ammoniated acetamide clusters

In the spectrum of acetamide clusters, the signals that were 17 and 18 mass units heavier than the masses of neat clusters [$m/z(\text{monomer})=59$] were detected; the peaks were located at m/z 76, 135 and m/z 77, 136, 195,

254, correspondingly. We assigned these fragments to be the products of the larger neat and protonated clusters that form via NH_3^+ migration within the cluster followed by the fragmentation and presented them in the form of $(\text{CH}_3\text{CONH}_2)_n\text{NH}_3^+$ and $(\text{CH}_3\text{CONH}_2)_n(\text{NH}_3)\text{H}^+$, respectively. This is a minority fragmentation pathway, as the intensity of these ions was weak. The protonated ammoniated cluster ions were found to appear in a certain energy window, which became narrower as the ion size increased (see Figure 22). At 11 eV, no such ions were detected.

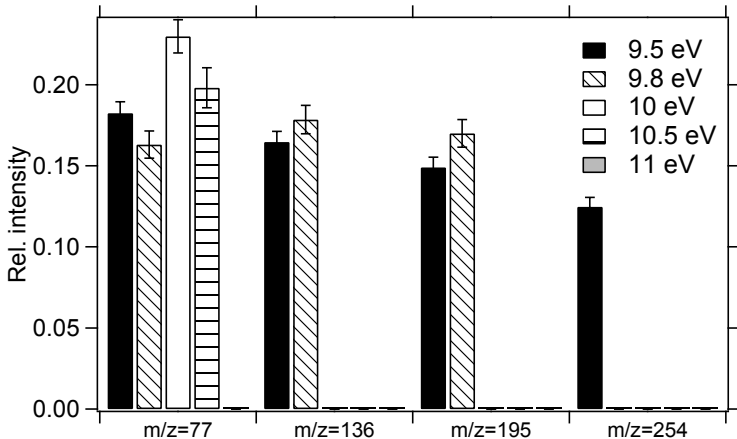


Figure 22: Distribution of $(\text{CH}_3\text{CONH}_2)_n(\text{NH}_3)\text{H}^+$ ($n=1-4$ for m/z 77, 136, 195, and 254, correspondingly) ions as a function of photon energy. Normalized to the protonated trimer signal.

We proposed a two-step formation mechanism for the ammoniated ions. The first step is hydrogen migration within the ionized monomer from the methyl group to the amino group. The second step is NH_3^+ transfer to a neighboring neutral monomer with the breakage of one C-N bond and one hydrogen bond. As a result of this reaction, neutral ethenone (CH_2CO) is released, and a $(\text{CH}_3\text{CONH}_2)_n(\text{NH}_3)^+$ ion is formed. We calculated the potential energy surface of these processes on the example of ionized acetamide dimer. The hydrogen transition path is shown on the left-hand side of Figure 23. The reaction starts from S3, then follows two closely located transition states (TS1, TS2) and ends in S1. The calculation predicts about 1.5 eV energy barrier for hydrogen transfer. The right-hand side of Figure 23 explores the ammoniated acetamide ion formation by dissociation of one C-N bond and one hydrogen bond. This step requires 1.84 eV energy from the lowest-energy ionic geometry (S1). The formation of S1 in the exothermic process is energetically more favorable. However, endothermic reaction leading to the ammoniated acetamide is feasible if

there is enough excess energy after surpassing the transition states.

Calculation shows that in ammoniated acetamide, the NH_3 moiety connects through $\text{O}-\text{H}\cdots\text{N}-\text{H}_2$ hydrogen bond. This could explain why these ions are not seen at higher photon energies. If a large amount of energy is deposited on the cluster, not only it facilitates the transfer of hydrogen from methyl to amino group and formation of ammoniated cluster ion, but also it facilitates its further dissociation by breaking the hydrogen bond to produce protonated species and NH_2 .

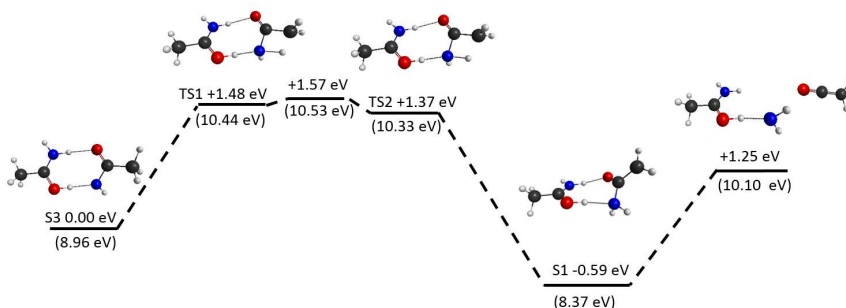


Figure 23: Potential energy surface of hydrogen migration from a methyl to amino group in acetamide dimer ion. The right-hand side explores a dissociation reaction yielding ammoniated monomer ions. Energy values in parenthesis are with respect to the neutral dimer. Zero-point energies are included.

In the same way, NH_3^+ transfer is possible in protonated clusters. Intermolecular proton transfer reactions lead to the rearrangement of the monomers within the cluster ion to accommodate the newly formed structure. In this process, excess energy could release, facilitating subsequent dissociative NH_3^+ transfer that leads to the formation of protonated-ammoniated cluster ion.

Experimentally, the appearance energy of a mixture of ammoniated acetamide and its protonated form was determined to be 9.28 ± 0.06 eV (see Paper IV), which within error bars equals to that of the neat and protonated dimer ions (9.36 ± 0.03 and 9.24 ± 0.03 eV, respectively). This supports the assessment of these fragments as secondary fragmentation products of larger clusters with lower appearance energy.

Interestingly, the intramolecular NH_3^+ transfer within single acetamide molecule from one carbon to another upon photoionization was also detected and reported earlier [67, 68]. Thus, single molecule property was transferred to the cluster system.

4.2.4 Photofragmentation depending on the clustering condition

In the case of acetic acid clusters, two PIY experiments were performed with different clustering conditions in the photon energy range 9-11.3 eV with 0.05 eV energy step. The goal of these experiments was to investigate the effect of clustering conditions on the distribution, structure and/or internal energy of the clusters. Two parameters were changed: the nozzle diameter and nozzle-skimmer distance. In experiment A, a nozzle with a diameter of 18 μm was used, and the distance between skimmer and nozzle was 12.5 mm. In experiment B, a nozzle with a smaller diameter of 7 μm was used, and the skimmer-nozzle distance was shortened by 2.5 mm. Reducing the nozzle size from experiment A to B, resulted in the increase of the source pressure by about 40 times. Therefore, a cooling efficiency was enhanced in experiment B by increasing the number of collisions during expansion through a smaller nozzle. During strong expansion, small clusters (dimers, trimers) could achieve very low temperatures and therefore lower internal energies [24].

In Figure 24, the intensities of the peaks detected in the mass spectra of experiments A and B are placed together for easy comparison. Clearly, varying the clustering conditions has a significant effect on the distribution of fragments: The signal of larger cluster ions is much higher in experiment B. Also, a peak at m/z 105, which is the fragment of the dimer is strong in experiment B, suggesting the higher neutral dimer fraction. Thus, the clustering conditions of experiment B were more favorable for the cluster formation due to more efficient cooling. However, one important change that cannot be explained by the mass distribution shift in the neutral cluster ensemble is the detection of neat acetic acid dimer positive ions at m/z 120 in experiment B, but not in experiment A. More likely, this is evidence of internal changes in cluster geometry and/or energy, which is very significant from the viewpoint of physical insight but would require further dedicated studies to characterize it in more detail.

To shed more light on the formation of neat dimer ions, we measured four mass spectra at 10.75 eV slightly varying clustering conditions such as expansion chamber pressure (by increasing the carrier gas pressure) and nozzle-skimmer distance, while using a nozzle with 7 μm diameter (see Figure 25).

The ratios of the neat to the protonated dimer are 1.44, 1.67, 4.85, and 3.87 in the spectra from 1 to 4, correspondingly. Comparing the spectra measured with the same pressure and different skimmer-nozzle distances, it is evident that the change in the expansion chamber pressure influences the ratio more than the change in the skimmer-nozzle distance. An increase in the expansion chamber pressure (P_{exp}) from 1.3×10^{-4} to 2×10^{-4} mbar results in the suppression of the protonated dimer and protonated

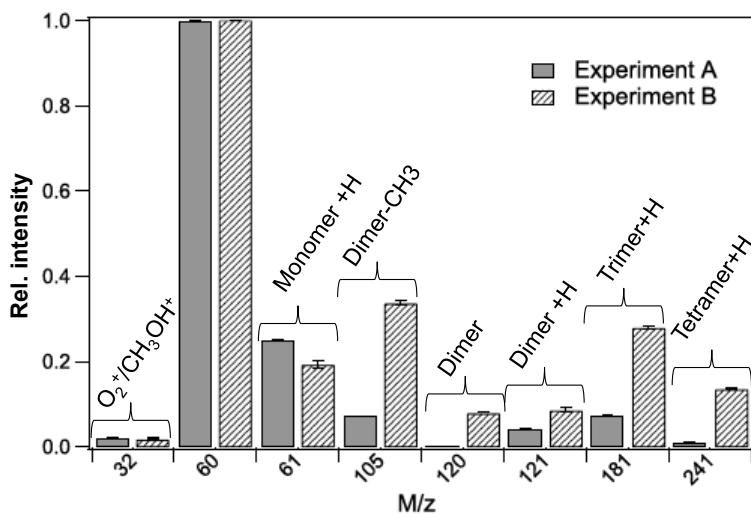


Figure 24: Intensities of the acetic acid cluster peaks detected in two partial ion yield experiments (A and B) in the photon energy range of 9-11.3 eV. Normalized to monomer signal.

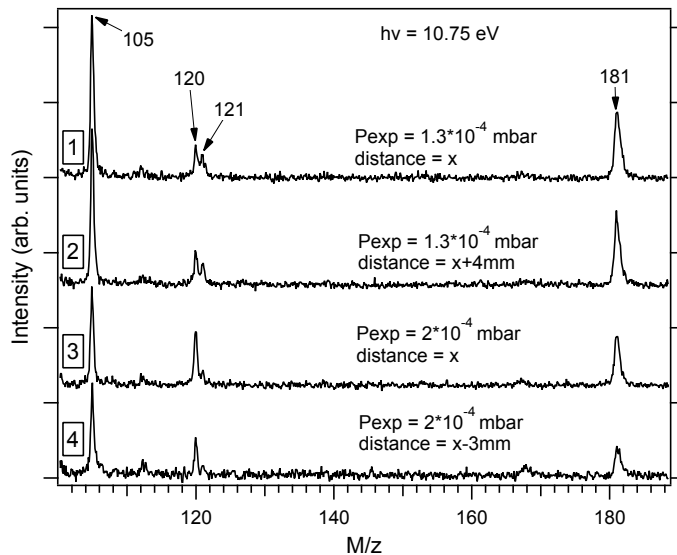


Figure 25: Mass spectra of acetic acid clusters formed at different clustering conditions. All spectra were measured at 10.75 eV. Expansion chamber pressure (Pexp) and the skimmer-nozzle distances ($x=12.5$ mm) were varied. Spectra are normalized to recording time.

trimer signals but an increase in the neat dimer signal. This trend is consistent with the changes observed from experiment A to B, as here we move towards higher carrier gas pressure conditions (in experiment B, $P_{exp} = 1.2 \times 10^{-4}$ mbar) and stronger cooling, although in a smaller step than by reducing the nozzle size. The decrease in protonated clusters signal at strong expansion conditions indicates that intermolecular proton transfer reactions are suppressed if produced clusters have very low temperatures and thus low internal energies. Consequently, ionized dimers, trimers and larger clusters retain their neutral geometry up to the moment of hydrogen bond breakage and then dissociate by the loss of some amount of monomer units before proton transfer takes place. So, the neat dimer ions might be formed from trimer dissociation by the loss of one monomer or from tetramer dissociation by the loss of two monomer units. This assumption is supported by the computational result which predicts a significant energy barrier of 1.11 eV for reaching the optimal low-energy dimer ion geometries by the hydrogen migration from the methyl group that naturally would produce protonated monomers (see Paper IV, Theory). Therefore, the high-energy geometries that produce neat species are mostly formed in better nucleation conditions. Thus, the exact conditions of the dimer ion formation and also fragmentation processes play a crucial role.

In conclusion, in acetic acid clusters, we observed fragmentation that depends on clustering condition. In light of our experimental and computational results, we suggest that stronger expansion conditions result in larger cluster sizes and in lower cluster temperatures. Clusters with lower internal energy are less likely to overcome the energy barrier to reach the optimal geometry prior to dissociation. Thus, the production of unprotonated species is facilitated. Therefore, with a systematic study over a broad range of expansion conditions, such dissociation that depends on the clustering condition might be a more detailed probe into geometries of the cluster ions.

Conclusions

The vacuum ultraviolet mass spectrometric study revealed rich dissociation dynamics in ionic and hydrogen-bonded compounds of organic origin. Studied molecules, ionic 1-ethyl-3-methylimidazolium tetrafluoroborate (EMImBF₄) and hydrogen-bonded dimers of acetamide, (CH₃CONH₂)₂, and acetic acid, (CH₃COOH)₂, have common trends in dissociation behaviour. First, they dissociate by breaking the bonds that hold together two counterparts of the molecule: cation + anion in ionic liquid and two monomer subunits in molecular dimers. Ionic liquid was shown to break apart via charge separation already below the ionization threshold as a result of dissociative excitation. The second common trend is dissociation after transferring atom(s) from one counterpart to another. In clusters, the dominant fragmentation pathway is proton migration from ionized monomer subunit to the neutral one that results in the formation of protonated clusters. In acetamide clusters, the dissociative transfer of NH₃⁺ moiety is occurring that results in the formation of ammoniated clusters. In ionic liquid, the fragment such as dehydrogenated EMImF⁺ forms by exchanging the cation's proton to anion's fluorine.

Photoelectron spectroscopy study of EMImBF₄ combined with density of states calculations using two different computational methods revealed the evidence of electronic relaxation. Strong relaxation of the electronic structure was shown to be occurring in the inner valence states of the cation, while no significant relaxation in the anion and the outer valence states of the cation was observed.

Mass spectrometry was shown to be useful outside of its main domain – detection of ions. Experiments with partly deuterated acetamide clusters not only determined the exact proton transfer path in proton transfer reactions but provided information also on the geometry of neutral acetamide dimer.

A significant finding is that not only photon energy influences the outcome of the valence ionization (at higher photon energy new fragmentation channels open up), but also the conditions at which the samples are introduced into the gas phase. In the case of acetic acid clusters, different clustering conditions resulted in different mass spectra. A conclusion is drawn that photofragmentation channels of a molecule depend on its internal energy. Lower internal energy suppresses atomic rearrangements that might be required for a particular fragment formation, and instead, a new fragment is formed that does not require any reorganization of the system. We observed such behaviour for acetic acid trimer that starts producing unprotonated dimers at stronger expansion conditions (lower internal energy), while there were no unprotonated dimers produced at weaker expansion conditions (higher internal energy).

In the future, systematic studies on the effect of clustering conditions on the structure, energy, cluster size distribution and photofragmentation pathways of molecular clusters are required to deepen the understanding of clusters' chemistry.

Summary in Estonian

Ioonsete ja vesiniksidemetega molekulide fragmenteerumine sünkrotronkiirguse mõjul

Käesolevas töös uuriti eksperimentaalselt ja arvutuslikult fragmenteerumisprotsesse ioonsetes ja vesiniksidemetega seotud molekulides. Uurimisobjektiks oli neli proovi: ioonne vedelik 1-etüül-3-metüülimidasoolium tetrafluoroboraat (EMImBF_4) ja vesiniksidemetega seotud molekulaarsed klastrid atsetamiidist (CH_3CONH_2), atsetamiid-2,2,2-d3-st (CD_3CONH_2) ja äädikhapest (CH_3COOH). Klastrite uuringutes keskenduti dimeeridele.

Antud teadustöö eesmärgiks oli uurida footoni energia mõju proovide stabiilsusele ja fragmenteerumismehhanismidele. Gaasfaasis olevate molekulide ioniseerimiseks kasutati sünkrotron- või gaaslahenduslambi kiirgust vaakumultavioleti piirkonnas. Eksperimendid sooritati sünkrotronkiirguse keskuses MAX-lab (Lund, Rootsi) ja Turu Ülikooli materjalide uurimislaboris. Kõiki proove uuriti massispektromeetria abil, ioonne vedelik oli täiendavalt uuritud fotoelektronspektroskoopia abil. Erinevate fragmenteerumiskanalite energetiliste omaduste välja selgitamiseks mõõdeti ioonide osasaagised.

Näidati, et mõlemad uuritud ühenditüübid kipuvad ulatuslikult fragmenteeruma vaakumultavioletkiirguse mõjul. Peamised fragmendid ioonse vedeliku massispektris olid EMIm^+ kation ja selle fragmentatsiooni produktid — ioonid, mis tekivad kui EMIm^+ kaotab kas ühe oma alküülrühmadest, mõlemad alküülrühmad või jaguneb fragmentideks imidasooliumi rõnga purunemisel. Samuti detekteeriti ioone nagu EMImF^+ ja EMImBF_2^+ , mis tekkisid aniooni ja katiooni aatomite ümberorganiseerumisel enne fragmenteerumist.

Peamised fragmenteerumisprotsessid äädikhape ja atsetamiidi klastrite puhul olid monomeeride dissotsieerumine klastrilt vesiniksidemete katkemisel, dissotsiatiivne prootoni ülekanne ioniseeritud monomeerilt neutraalsele naabrile ning monomeeride dissotsieerumine protoneeritud klastritelt. Lisaks detekteeriti fragmenteerumiskanaleid, mis otseselt sõltuvad monomeeride struktuurist: dissotsiatiivne NH_3^+ ülekanne atsetamiidi klastrites ja äädikhappe dimeerile iseloomulik metüülrühma eraldumine.

Kogutud andmete põhjal selgitati välja, et ioonsed ja vesiniksidemetega seotud molekulid fragmenteervad väga sarnaselt. Näiteks, kui võrrelda dissotsiatsiooniprotsesse molekulaarsetes dimeerides ja ioonses vedelikus, siis esimene sarnasus seisneb selles, et sellised molekulaarsed süsteimid dissotsieeruvad süsteemi kahte koostisosa kokkuhoidvate sidemete katkemisel. Seega, ioonne vedelik laguneb katiooniks ja aniooniks

ning molekulaarsed dimeerid – kaheks monomeeriks. Näidati, et ioonne vedelik fragmenteerub enda koostisosadeks juba allpool ioniseerimisläve dissotsiatiivse fotoergastuse tulemusena. Teine ühine fragmentatsioonimehhanism on fragmenteerumine pärast aatomite üleminekut ühelt koostisosalt teisele. Klastrites domineerivaks fragmentatsioonikanaliks on prootoni üleminek ioniseeritud monomeerilt neutraalsele naabrile, mille tulemusena tekivad protoneeritud klastrid. Katsed osaliselt deutereeritud atsetamiidi klastritega näitasid, et domineerivaks prootoni allikaks on aminorühm. Ioonse vedeliku korral täheldati, et fotoneeldumise tulemusena toimub katiooni vesiniku aatomi ümbervahetus aniooni fluori aatomiga, mille tulemusena tekib EMI^+F^- fragment.

Olulise aspektina võib välja tuua, et erinevate fragmentatsioonikanalite esinemine ei sõltu mitte ainult footoni energiast, vaid on tugevalt mõjutatud ka uuritava molekuli klasterisatsiooni tingimustest. Äädikhappe klastrite korral erinevad klasterisatsiooni tingimused põhjustasid erinevusi massispektrites. Sellest võib järeldada, et fragmentatsiooni kanalid sõltuvad ka molekulide siseenergiast. Madalama siseenergiaga molekulaarsetes süsteemides on alla surutud aatomite ümberpaigutamisprotsessid, mille tulemusena võivad tekkida uued fragmendid, kuna aatomite liikumist süsteemis ei toimunud. Selline käitumine oli iseloomulik madalama siseenergiaga äädikhappe trimeerile, mis fragmenteerus enne prootoni ülekannet vesiniksidemete lõhkumisel, et moodustada dimeeri ioone. Kõrgematel siseenergiatel aga selline fragmentatsioonikanal puudus. Klasterisatsiooni tingimuste mõju klastrite suuruse jaotusele, energiatele, struktuuridele ning fragmentatsioonikanalitele vajab täiendavat süstemaatilist uurimist.

Acknowledgements

This thesis was made under joint supervision of Tartu and Turku Universities. Many people contributed to the completion of this work and now it is time to say thank you.

Firstly, I find myself in need of thanking my supervisors – Prof. Ergo Nõmmiste, Prof. Edwin Kukk and Dr. Kuno Kooser, without whom this work would not be possible. I am proud to have an opportunity to work with them. All of them did a wonderful job guiding and helping me out during my PhD studies. I am thankful to Ergo for his support in all of my scientific undertakings. A special thanks for introducing me to the synchrotron measurements back in 2013. Edwin deserves high praise for his efforts of making me a better writer. His feedback on my manuscripts was invaluable. Also, I am grateful that Edwin involved me in many of his beamtimes at Max-lab, SOLEIL and SACLA, so I could develop new skills and think outside of my PhD project. Kuno deserves many-many thanks for constructing the cluster source used in this work and his explicit explanations concerning the cluster experiments and data analysis. He is a good teacher always eager to help no matter what time of the day it is.

Secondly, I am grateful to all co-authors of the thesis-included and not included papers as I learned something useful from all of them. Especially, I am thankful to Dr. Ivar Kuusik and to our graduate student Hanna Myllynen, who performed computational work to support the experimental findings in the studies of ionic liquid and clusters, correspondingly. In addition, my thanks go out to Tartu University colleagues – Dr. Jaanus Kruusma and Arvo Tõnisoo for the help and support during my first beamtimes and to our graduate student Meeri Lembinen for many fruitful discussions.

Thirdly, I am thankful to my good friend (or should I say my older sister?) Dr. Helena Levola, the meeting with whom greatly affected the direction of my PhD studies by connecting me to the materials research group of Turku University. You are a great support and inspiration.

Thank you to my Turku University colleagues – Dr. Sari Granroth, Dr. Dang Trinh Ha, Dr. Johannes Niskanen, and Dr. Eero Itälä for always finding time to help me solve some minor and not too minor problems.

Finally, I am thankful to my family and friends for their continued encouragement and support. In particular to my mother, Olga, and my brother, Mark, who always believe in me and love me no matter what.

And last but definitely not least, my thanks go out to my husband, Artjom. Thank you for everything. Especially for keeping me sane at the times of difficulty. I love you.

References

- [1] Iso 21348 definitions of solar irradiance spectral categories. http://www.spacewx.com/pdf/SET_21348_2004.pdf. Accessed: 11.01.2018.
- [2] M. Born and R. Oppenheimer. Zur quantentheorie der molekeln. *Annalen der Physik*, 389(20):457–484, March 1927.
- [3] I. N. Levine. *Quantum Chemistry*. Pearson, 2014. Google-Books-ID: dvyJMQEACAAJ.
- [4] E. G. Lewars. *Computational chemistry: Introduction to the theory and applications of molecular and quantum mechanics*. Springer Netherlands, 2nd edition, 2011.
- [5] H. Hertz. Ueber einen einfluss des ultravioletten lichtes auf die electrische entladung. *Annalen der Physik*, 267(8):983–1000, March 1887.
- [6] A. Einstein. Über einen die erzeugung und verwandlung des lichtes betreffenden heuristischen gesichtspunkt. *Annalen der Physik*, 322(6):132–148, March 1905.
- [7] T. Koopmans. Über die zuordnung von wellenfunktionen und eigenwerten zu den einzelnen elektronen eines atoms. *Physica*, 1(1):104–113, January 1934.
- [8] G. Schönhense and U. Heinzmann. A capillary discharge tube for the production of intense vuv resonance radiation. *Journal of Physics E: Scientific Instruments*, 16(1):74, 1983.
- [9] H. Wiedemann. *Particle accelerator physics*. Springer, Berlin, Heidelberg, 2007. DOI: 10.1007/978-3-540-49045-6_1.
- [10] P. Duke. *Synchrotron radiation: Production and properties*. Oxford University Press, Oxford ; New York, February 2009.
- [11] D. Attwood and A. Sakdinawat. *X-Rays and extreme ultraviolet radiation: Principles and applications*. Cambridge University Press, December 2016.
- [12] F. R. Elder, R. V. Langmuir, and H. C. Pollock. Radiation from electrons accelerated in a synchrotron. *Physical Review*, 74(1):52–56, July 1948.

- [13] P. Willmott. *An introduction to synchrotron radiation: Techniques and applications*. John Wiley & Sons, Ltd, 2011. DOI: 10.1002/9781119970958.
- [14] M. Bässler, A. Ausmees, M. Jurvansuu, R. Feifel, J. O. Forsell, P. de Tarso Fonseca, A. Kivimäki, S. Sundin, S. L. Sorensen, R. Nyholm, O. Björneholm, S. Aksela, and S. Svensson. Beam line I411 at MAX II – performance and first results. *Nuclear Instruments and Methods in Physics Research Section A: Accelerators, Spectrometers, Detectors and Associated Equipment*, 469(3):382–393, August 2001.
- [15] S. Urpelainen, M. Huttula, T. Balasubramanian, R. Sankari, P. Kovala, E. Kukk, E. Nömmiste, S. Aksela, R. Nyholm, and H. Aksela. FINEST: a high performance branch-line for VUV photon energy range gas phase studies at MAX-lab. *AIP Conference Proceedings*, 1234(1):411–414, June 2010.
- [16] T. Balasubramanian, B. N. Jensen, S. Urpelainen, B. Sommarin, U. Johansson, M. Huttula, R. Sankari, E. Nömmiste, S. Aksela, H. Aksela, R. Nyholm, R. Garrett, I. Gentle, K. Nugent, and S. Wilkins. The normal incidence monochromator beamline I3 on MAX III. *AIP Conference Proceedings*, 1234(1):661–664, June 2010.
- [17] M. Bässler, J.-. O. Forsell, O. Björneholm, R. Feifel, M. Jurvansuu, S. Aksela, S. Sundin, S. L. Sorensen, R. Nyholm, A. Ausmees, and S. Svensson. Soft X-ray undulator beam line I411 at MAX-II for gases, liquids and solid samples. *Journal of Electron Spectroscopy and Related Phenomena*, 101:953–957, June 1999.
- [18] J. Gross. *Mass spectrometry - a textbook*. Springer-Verlag Berlin Heidelberg, 2004.
- [19] W. C. Wiley and I. H. McLaren. Time-of-Flight mass spectrometer with improved resolution. *Review of Scientific Instruments*, 26(12):1150–1157, December 1955.
- [20] J. H. D. Eland. *Photoelectron spectroscopy: an introduction to ultraviolet photoelectron spectroscopy in the gas phase*. Butterworths, 1974.
- [21] D. Roy and D. Tremblay. Design of electron spectrometers. *Reports on Progress in Physics*, 53(12):1621, 1990.
- [22] N. Mårtensson, P. Baltzer, P. A. Brühwiler, J. O. Forsell, A. Nilsson, A. Stenborg, and B. Wannberg. A very high resolution electron spectrometer. *Journal of Electron Spectroscopy and Related Phenomena*, 70(2):117–128, December 1994.

- [23] S. K. Kim, W. Lee, and D. R. Herschbach. Cluster beam chemistry: Hydration of nucleic acid bases; Ionization potentials of hydrated adenine and thymine. *The Journal of Physical Chemistry*, 100(19):7933–7937, January 1996.
- [24] H. Pauly. *Atom, molecule, and cluster beams II: Cluster beams, fast and slow beams, accessory equipment and applications*. Springer Science & Business Media, September 2000. Google-Books-ID: py4Jrrsr6TUC.
- [25] H. Pauly. *Atom, Molecule, and Cluster Beams I: Basic Theory, Production and Detection of Thermal Energy Beams*. Springer Series on Atomic, Optical, and Plasma Physics. Springer-Verlag, Berlin Heidelberg, 2000.
- [26] E. Kukk, K. Ueda, U. Hergenhahn, X.-J. Liu, G. Prümper, H. Yoshida, Y. Tamenori, C. Makochekeanwa, T. Tanaka, M. Kitajima, and H. Tanaka. Violation of the Franck-Condon principle due to recoil effects in high energy molecular core-level photoionization. *Physical Review Letters*, 95(13):133001, September 2005.
- [27] E. Kukk, G. Snell, J. D. Bozek, W.-T. Cheng, and N. Berrah. Vibrational structure and partial rates of resonant Auger decay of the N 1s \rightarrow 2 π core excitations in nitric oxide. *Physical Review A*, 63(6):062702, May 2001.
- [28] I. Velchev, W. Hogervorst, and W. Ubachs. Precision VUV spectroscopy of Ar I at 105 nm. *Journal of Physics B: Atomic, Molecular and Optical Physics*, 32(17):L511, 1999.
- [29] P. Wasserscheid and T. Welton. *Ionic liquids in synthesis, 2nd edition*. Wiley-VCH Verlag GmbH & Co. KGaA, 2007.
- [30] J. S. Wilkes, J. A. Levisky, R. A. Wilson, and C. L. Hussey. Dialkylimidazolium chloroaluminate melts: a new class of room-temperature ionic liquids for electrochemistry, spectroscopy and synthesis. *Inorganic Chemistry*, 21:1263–1264, 1982. DOI: 10.1021/ic00133a078.
- [31] J. S. Wilkes and M. J. Zaworotko. Air and water stable 1-ethyl-3-methylimidazolium based ionic liquids. *Journal of the Chemical Society, Chemical Communications*, 0(13):965–967, January 1992.
- [32] D. D. Patel and J.-M. Lee. Applications of ionic liquids. *Chemical Record (New York, N.Y.)*, 12(3):329–355, June 2012.

- [33] R. L. Vekariya. A review of ionic liquids: Applications towards catalytic organic transformations. *Journal of Molecular Liquids*, 227:44–60, February 2017.
- [34] C. Siimenson, M. Lembinen, O. Oll, L. Läll, M. Tarkanovskaja, V. Ivaništšev, L. Siinor, T. Thomberg, K. Lust, and E. Lust. Electrochemical investigation of 1-ethyl-3-methylimidazolium bromide and tetrafluoroborate mixture at Bi(111) electrode interface. *Journal of The Electrochemical Society*, 163(9):H723–H730, January 2016.
- [35] M. Tarkanovskaja, R. Vålbe, K. Põhako-Esko, U. Mäeorg, V. Reedo, A. Hoop, K. Saal, A. Krumme, I. Kink, I. Heinmaa, and A. Lõhmus. Novel homogeneous gel fibers and capillaries from blend of titanium tetrabutoxide and siloxane functionalized ionic liquid. *Ceramics International*, 40(6):7729–7735, July 2014.
- [36] R. Vålbe, M. Tarkanovskaja, U. Mäeorg, V. Reedo, A. Hoop, I. Kink, and A. Lõhmus. Elaboration of hybrid cotton fibers treated with an ionogel/carbon nanotube mixture using a sol-gel approach. *Open Chemistry*, 13(1), 2014.
- [37] R. Vålbe, R. Lõhmus, U. Mäeorg, M. Umalas, V. Reedo, M. Tarkanovskaja, A. Lõhmus, and J. Kübarsepp. A method for preparing metal oxide nanoparticles in a gel. Patent number: EE 201500022 A; Priority date: 18.06.2014.
- [38] R. Vålbe, M. Tarkanovskaja, U. Mäeorg, V. Reedo, A. Lõhmus, T. Taaber, S. Vlassov, and R. Lõhmus. Phosphonium-based ionic liquids mixed with stabilized oxide nanoparticles as highly promising lubricating oil additives. *Proceedings of the Estonian Academy of Sciences*, 66(2):174, 2017.
- [39] M. J. Earle, J. M. S. S. Esperança, M. A. Gilea, J. N. C. Lopes, L. P. N. Rebelo, J. W. Magee, K. R. Seddon, and J. A. Widegren. The distillation and volatility of ionic liquids. *Nature*, 439(7078):831–834, February 2006.
- [40] J. P. Leal, J. M. S. S. Esperança, M. E. Minas da Piedade, J. N. Canongia Lopes, L. P. N. Rebelo, and K. R. Seddon. The nature of ionic liquids in the gas phase. *The Journal of Physical Chemistry A*, 111(28):6176–6182, July 2007.
- [41] J. P. Armstrong, C. Hurst, R. G. Jones, P. Licence, K. R. J. Lovelock, C. J. Satterley, and I. J. Villar-Garcia. Vapourisation of ionic liquids. *Physical Chemistry Chemical Physics*, 9(8):982–990, February 2007.

- [42] D. Strasser, F. Goulay, M. S. Kelkar, E. J. Maginn, and S. R. Leone. Photoelectron spectrum of isolated ion-pairs in ionic liquid vapor. *The Journal of Physical Chemistry A*, 111(17):3191–3195, May 2007.
- [43] J. H. Gross. Molecular ions of ionic liquids in the gas phase. *Journal of the American Society for Mass Spectrometry*, 19(9):1347–1352, September 2008.
- [44] Y. Shao, L. F. Molnar, Y. Jung, J. Kussmann, C. Ochsenfeld, S. T. Brown, A. T. B. Gilbert, L. V. Slipchenko, S. V. Levchenko, D. P. O’Neill, R. A. D. Jr, R. C. Lochan, T. Wang, G. J. O. Beran, N. A. Besley, J. M. Herbert, C. Y. Lin, T. V. Voorhis, S. H. Chien, A. Sodt, R. P. Steele, V. A. Rassolov, P. E. Maslen, P. P. Korambath, R. D. Adamson, B. Austin, J. Baker, E. F. C. Byrd, H. Dachsel, R. J. Doerksen, A. Dreuw, B. D. Dunietz, A. D. Dutoi, T. R. Furlani, S. R. Gwaltney, A. Heyden, S. Hirata, C.-P. Hsu, G. Kedziora, R. Z. Khallilulin, P. Klunzinger, A. M. Lee, M. S. Lee, W. Liang, I. Lotan, N. Nair, B. Peters, E. I. Proynov, P. A. Pieniazek, Y. M. Rhee, J. Ritchie, E. Rosta, C. D. Sherrill, A. C. Simmonett, J. E. Subotnik, H. L. W. Iii, W. Zhang, A. T. Bell, A. K. Chakraborty, D. M. Chipman, F. J. Keil, A. Warshel, W. J. Hehre, H. F. S. Iii, J. Kong, A. I. Krylov, P. M. W. Gill, and M. Head-Gordon. Advances in methods and algorithms in a modern quantum chemistry program package. *Physical Chemistry Chemical Physics*, 8(27):3172–3191, July 2006.
- [45] C. J. Koh and S. R. Leone. Simultaneous ion-pair photodissociation and dissociative ionization of an ionic liquid: velocity map imaging of vacuum-ultraviolet-excited 1-ethyl-3-methylimidazolium bis(trifluoromethylsulfonyl)imide. *Molecular Physics*, 110(15-16):1705–1712, August 2012.
- [46] R. Cooper, A. M. Zolot, J. A. Boatz, D. P. Sporleder, and J. A. Stearns. IR and UV spectroscopy of vapor-phase jet-cooled ionic liquid [emim][Tf₂N]: Ion pair structure and photodissociation dynamics. *The Journal of Physical Chemistry A*, 117(47):12419–12428, November 2013.
- [47] Y. Cao and T. Mu. Comprehensive investigation on the thermal stability of 66 ionic liquids by thermogravimetric analysis. *Industrial & Engineering Chemistry Research*, 53(20):8651–8664, May 2014.
- [48] H. Ohtani, S. Ishimura, and M. Kumai. Thermal decomposition behaviors of imidazolium-type ionic liquids studied by pyrolysis-gas chromatography. *Analytical Sciences: The International Journal of*

the Japan Society for Analytical Chemistry, 24(10):1335–1340, October 2008.

- [49] M. G. Freire, C. M. S. S. Neves, I. M. Marrucho, J. A. P. Coutinho, and A. M. Fernandes. Hydrolysis of tetrafluoroborate and hexafluorophosphate counter ions in imidazolium-based ionic liquids. *The Journal of Physical Chemistry A*, 114(11):3744–3749, March 2010.
- [50] A. W. Taylor, K. R. J. Lovelock, R. G. Jones, and P. Licence. Borane-substituted imidazol-2-ylidenes: syntheses in vacuo. *Dalton Transactions*, 40(7):1463–1470, February 2011.
- [51] M. C. Kroon, W. Buijs, C. J. Peters, and G.-J. Witkamp. Quantum chemical aided prediction of the thermal decomposition mechanisms and temperatures of ionic liquids. *Thermochimica Acta*, 465(1):40–47, December 2007.
- [52] O. Hollóczki, D. Gerhard, K. Massone, L. Szarvas, B. Németh, T. Veszprémi, and L. Nyulászi. Carbenes in ionic liquids. *New Journal of Chemistry*, 34(12):3004–3009, November 2010.
- [53] M. Reinmöller, A. Ulbrich, T. Ikari, J. Preiss, O. Höfft, F. Endres, S. Krischok, and W. J. D. Beenken. Theoretical reconstruction and elementwise analysis of photoelectron spectra for imidazolium-based ionic liquids. *Physical Chemistry Chemical Physics*, 13(43):19526–19533, November 2011.
- [54] R. L. Johnston. *Atomic and molecular clusters*. CRC Press, April 2002.
- [55] F. Puletti, G. Mallocci, G. Mulas, and C. Cecchi-Pestellini. Large prebiotic molecules in space: photophysics of acetic acid and its isomers. *Monthly Notices of the Royal Astronomical Society*, 402(3):1667–1674, March 2010.
- [56] D. T. Halfen, V. Ilyushin, and L. M. Ziurys. Formation of peptide bonds in space: A comprehensive study of formamide and acetamide in Sgr B2(N). *The Astrophysical Journal*, 743(1):60, December 2011.
- [57] S. R. Gadre, S. D. Yeole, and N. Sahu. Quantum chemical investigations on molecular clusters. *Chemical Reviews*, 114(24):12132–12173, December 2014.
- [58] C. Desfrancois, S. Carles, and J. P. Schermann. Weakly bound clusters of biological interest. *Chemical Reviews*, 100(11):3943–3962, November 2000.

- [59] M. W. Schmidt, K. K. Baldridge, J. A. Boatz, S. T. Elbert, M. S. Gordon, J. H. Jensen, S. Koseki, N. Matsunaga, K. A. Nguyen, S. Su, et al. General atomic and molecular electronic structure system. *Journal of computational chemistry*, 14(11):1347–1363, 1993.
- [60] Y. B. Pithawalla, C. Covington, I. McComish, I. N. Germanenko, and M. S. El-Shall. Comparative study of the binary clusters of acetic acid–water and acetic acid–benzene using electron impact and multiphoton ionization techniques. *International Journal of Mass Spectrometry*, 218(1):49–62, June 2002.
- [61] D. L. C. Emmeluth, M. A. Suhm. A monomers-in-dimers model for carboxylic acid dimers. *The Journal of Chemical Physics*, 118(5):2242–2255, January 2003.
- [62] Y. J. Hu, H. B. Fu, and E. R. Bernstein. Infrared plus vacuum ultraviolet spectroscopy of neutral and ionic ethanol monomers and clusters. *The Journal of Chemical Physics*, 125(15):154305, October 2006.
- [63] R. Sievert, I. Cadez, J. Van Doren, and A. W. Castleman. Mass spectral and electric deflection study of acetic acid clusters. *The Journal of Physical Chemistry*, 88(20):4502–4505, September 1984.
- [64] C. Y. Ng. *Vacuum ultraviolet photoionization and photodissociation of molecules and clusters*. WORLD SCIENTIFIC, June 1991. DOI: 10.1142/1244.
- [65] F. F. d. Silva, S. Jaksch, G. Martins, H. M. Dang, M. Dampc, S. Denifl, T. D. Märk, P. Limão-Vieira, J. Liu, S. Yang, A. M. Ellis, and P. Scheier. Electron attachment and electron ionization of acetic acid clusters embedded in helium nanodroplets. *Physical Chemistry Chemical Physics*, 11(48):11631–11637, December 2009.
- [66] M. Albrecht, C. A. Rice, and M. A. Suhm. Elementary peptide motifs in the gas phase: FTIR aggregation study of formamide, acetamide, N-methylformamide, and N-methylacetamide. *The Journal of Physical Chemistry. A*, 112(33):7530–7542, August 2008.
- [67] T. Drewello, N. Heinrich, W. P. M. Maas, N. M. M. Nibbering, T. Weiske, and H. Schwarz. Generation of the distonic ion $\text{CH}_2\text{NH}_3^{\bullet+}$: nucleophilic substitution of the ketene cation radical by ammonia and unimolecular decarbonylation of ionized acetamide. *Journal of the American Chemical Society*, 109(16):4810–4818, August 1987.

- [68] P. Mourgues, J. Chamot-Rooke, H. Nedev, and H.-E. Audier. Spontaneous and catalyzed isomerizations of the acetamide radical cation. *Journal of Mass Spectrometry*, 36(1):102–104, January 2001.

Original papers

CURRICULUM VITAE

Name: Marta Berholts (Tarkanovskaja)
Date of birth: 17.08.1989
Citizenship: Estonian
Address: W. Ostwaldi 1, 50411, Tartu, Estonia
E-mail: marta.berholts@ut.ee

Education:
2013–2018 Ph.D. studies in materials science, University of Tartu, University of Turku
2011–2013 M.Sc. in materials science, University of Tartu (*cum laude*)
2008–2011 B. Sc in materials science, University of Tartu
2005–2008 Sillamäe Kannuka Kool
1996–2005 Sinimäe Põhikool

Employment:
2010–2018 Laboratory assistant, University of Tartu
01.01.2018–31.05.2018 Doctoral student, University of Turku
15.10.2017–31.12.2017 Doctoral student, University of Turku

Professional training:
26.06–01.07.2016 66th Lindau Nobel Laureate Meeting in Physics, Lindau, Germany
29.03–29.04.2016 HERCULES European School, Neutrons and synchrotron radiation for science, Grenoble, France
19–27.05.2014 MAX IV Summer School In Synchrotron Radiation 2014 – Back To Basics, Lund, Sweden

List of publications:

1. Kuusik, I., **Tarkanovskaja, M.**, Kruusma, J., Reedo, V., Välbe, R., Lõhmus, A., Kisand, V., Lust, E., Kukk, E., and Nõmmiste, E. (2014). Near threshold photodissociation study of EMIMBF₄ vapor. RSC Adv. 5, 6834–6842.
2. Kuusik, I., **Tarkanovskaja, M.**, Kruusma, J., Kisand, V., Tõnisoo, A., Lust, E., and Nõmmiste, E. (2016). Valence band photoelectron spectra of [EMIM][BF₄] ionic liquid vapor: Evidences of electronic relaxation. Journal of Molecular Liquids 223, 939–942.
3. Levola, H., Itälä, E., Schlesier, K., Kooser, K., Laine, S., Laksman, J., Ha, D.T., Rachlew, E., **Tarkanovskaja, M.**, Tanzer, K., et al. (2015). Ionization-site effects on the photofragmentation of chloro- and bromoacetic acid molecules. Phys. Rev. A 92, 63409.

4. Siimenson, C., Lembinen, M., Oll, O., Läll, L., **Tarkanovskaja, M.**, Ivaništšev, V., Siinor, L., Thomberg, T., Lust, K., and Lust, E. (2016). Electrochemical Investigation of 1-Ethyl-3-methylimidazolium Bromide and Tetrafluoroborate Mixture at Bi(111) Electrode Interface. *J. Electrochem. Soc.* *163*, H723–H730.
5. **Tarkanovskaja, M.**, Välbe, R., Põhako-Esko, K., Mäeorg, U., Reedo, V., Hoop, A., Saal, K., Krumme, A., Kink, I., Heinmaa, I., et al. (2014). Novel homogeneous gel fibers and capillaries from blend of titanium tetrabutoxide and siloxane functionalized ionic liquid. *Ceramics International* *40*, 7729–7735.
6. Välbe, R., **Tarkanovskaja, M.**, Mäeorg, U., Reedo, V., Hoop, A., Kink, I., and Lõhmus, A. (2014). Elaboration of hybrid cotton fibers treated with an ionogel/carbon nanotube mixture using a sol-gel approach. *Open Chemistry* *13*.
7. **Tarkanovskaja, M.**, Kooser, K., Levola, H., Nõmmiste, E., and Kuk, E. (2016). Photoinduced intermolecular dynamics and subsequent fragmentation in VUV-ionized acetamide clusters. *The Journal of Chemical Physics* *145*, 124313.
8. Välbe, R., **Tarkanovskaja, M.**, Mäeorg, U., Reedo, Lõhmus, A., Taaber, T., Järvekülg, M., Vlassov, S., Lõhmus, R. (2017). Phosphonium-based ionic liquids mixed with stabilized oxide nanoparticles as highly promising lubricating oil additives. *Proceedings of the Estonian Academy of Sciences*, *66(2):174*, 10.3176/proc.2017.2.05
9. **Berholts, M.**, Myllynen, H., Kooser, K., Granroth, S., Itälä, E., Levola, H., Laksman, J., Oghbaee, S., Oostenrijk, B., Nõmmiste, E., Kuk, E. Photo-fragmentation of gas-phase acetic acid and acetamide clusters in the vacuum ultraviolet region. *The Journal of Chemical Physics* *147(19): 194302*.
10. Oras, S., Vlassov, S., **Berholts, M.**, Lõhmus, R., Mougine, K. Tuning adhesion forces between functionalized gold colloidal nanoparticles and silicon AFM tips: Role of ligands and capillary forces. Submitted to *Belstein Journal of Nanotechnology* in november 2017.

Patents:

1. Välbe, R., Lõhmus R., Mäeorg, U., Umalas, M., Reedo, V., **Tarkanovskaja, M.**, Lõhmus, A., Kübarsepp, J. A method for preparing metal oxide nanoparticles in a gel. Patent number: EE201500022 A, priority date: 18.06.2014.

ELULOOKIRJELDUS

Nimi: Marta Berholts (Tarkanovskaja)
Sünniaeg: 17.08.1989
Kodakondsus: Eesti
Aadress: W. Ostwaldi 1, 50411, Tartu, Estonia
E-post: marta.berholts@ut.ee

Haridus:
2013–2018 Doktoriõpe materjaliteaduses, Tartu Ülikool, Turu Ülikool
2011–2013 Magistriõpe materjaliteaduses, Tartu Ülikool (*cum laude*)
2008–2011 Bakalaureuseõpe materjaliteaduses, Tartu Ülikool
2005–2008 Sillamäe Kannuka Kool
1996–2005 Sinimäe Põhikool

Teenistuskäik:
2010–2018 Laborant, Tartu Ülikool
01.01.2018–31.05.2018 Doktorant, Tartu Ülikool
15.10.2017–31.12.2017 Doktorant, Tartu Ülikool

Erialane enesetäiendus:
26.06–01.07.2016 Nobeli preemia laureaate ja noortedlaste foorum füüsikas, Lindau, Saksamaa
29.03–29.04.2016 HERCULES Euroopa kool, neutroonid ja sünkrotronkiirgus teaduses, Grenoble, Prantsusmaa
19–27.05.2014 MAX IV suvekool sünkrotronkiirguses, Lund, Rootsi

Teaduspublikatsioonide loetelu:

1. Kuusik, I., **Tarkanovskaja, M.**, Kruusma, J., Reedo, V., Välbe, R., Lõhmus, A., Kisand, V., Lust, E., Kukk, E., and Nõmmiste, E. (2014). Near threshold photodissociation study of EMIMBF₄ vapor. RSC Adv. 5, 6834–6842.
2. Kuusik, I., **Tarkanovskaja, M.**, Kruusma, J., Kisand, V., Tõnisoo, A., Lust, E., and Nõmmiste, E. (2016). Valence band photoelectron spectra of [EMIM][BF₄] ionic liquid vapor: Evidences of electronic relaxation. Journal of Molecular Liquids 223, 939–942.
3. Levola, H., Itälä, E., Schlesier, K., Kooser, K., Laine, S., Laksman, J., Ha, D.T., Rachlew, E., **Tarkanovskaja, M.**, Tanzer, K., et al. (2015). Ionization-site effects on the photofragmentation of chloro- and bromoacetic acid molecules. Phys. Rev. A 92, 63409.
4. Siimenson, C., Lembinen, M., Oll, O., Läll, L., **Tarkanovskaja, M.**, Ivaništšev, V., Siinor, L., Thomberg, T., Lust, K., and Lust, E. (2016).

Electrochemical Investigation of 1-Ethyl-3-methylimidazolium Bromide and Tetrafluoroborate Mixture at Bi(111) Electrode Interface. *J. Electrochem. Soc.* *163*, H723–H730.

5. **Tarkanovskaja, M.**, Välbe, R., Põhako-Esko, K., Mäeorg, U., Reedo, V., Hoop, A., Saal, K., Krumme, A., Kink, I., Heinmaa, I., et al. (2014). Novel homogeneous gel fibers and capillaries from blend of titanium tetrabutoxide and siloxane functionalized ionic liquid. *Ceramics International* *40*, 7729–7735.
6. Välbe, R., **Tarkanovskaja, M.**, Mäeorg, U., Reedo, V., Hoop, A., Kink, I., and Lõhmus, A. (2014). Elaboration of hybrid cotton fibers treated with an ionogel/carbon nanotube mixture using a sol-gel approach. *Open Chemistry* *13*.
7. **Tarkanovskaja, M.**, Kooser, K., Levola, H., Nõmmiste, E., and Kuk, E. (2016). Photoinduced intermolecular dynamics and subsequent fragmentation in VUV-ionized acetamide clusters. *The Journal of Chemical Physics* *145*, 124313.
8. Välbe, R., **Tarkanovskaja, M.**, Mäeorg, U., Reedo, Lõhmus, A., Taaber, T., Järvekülg, M., Vlassov, S., Lõhmus, R. (2017). Phosphonium-based ionic liquids mixed with stabilized oxide nanoparticles as highly promising lubricating oil additives. *Proceedings of the Estonian Academy of Sciences*, *66(2):174*, 10.3176/proc.2017.2.05
9. **Berholts, M.**, Myllynen, H., Kooser, K., Granroth, S., Itälä, E., Levola, H., Laksman, J., Oghbaee, S., Oostenrijk, B., Nõmmiste, E., Kuk, E. Photo-fragmentation of gas-phase acetic acid and acetamide clusters in the vacuum ultraviolet region. *The Journal of Chemical Physics* *147(19): 194302*.
10. Oras, S., Vlassov, S., **Berholts, M.**, Lõhmus, R., Mougine, K. Tuning adhesion forces between functionalized gold colloidal nanoparticles and silicon AFM tips: Role of ligands and capillary forces. Submitted to *Belstein Journal of Nanotechnology* in november 2017.

Patentsed leiutised:

1. Välbe, R., Lõhmus R., Mäeorg, U., Umalas, M., Reedo, V., **Tarkanovskaja, M.**, Lõhmus, A., Kübarsepp, J. A method for preparing metal oxide nanoparticles in a gel. Patent number: EE201500022 A, priority date: 18.06.2014.

DISSERTATIONES SCIENTIAE MATERIALIS UNIVERSITATIS TARTUENSIS

1. **Martin Järvekülg.** Tubular microstructures by Hf-, Zr- and Ti-butoxide gel sheet rolling. Tartu, 2011, 112 p.
2. **Sergei Vlassov.** Investigation of nanoscale interactions and mechanical properties of nanostructures using quartz tuning fork based real-time measurements. Tartu, 2011, 171 p.
3. **Margus Kodu.** Pulsed Laser Deposition of Magnesium Oxide and Barium Ternary Oxides for Plasma Display Protective Layers. Tartu, 2011, 89 p.
4. **Rainer Pärna.** Surface studies of some oxide films. Tartu, 2011, 129 p.
5. **Jevgeni Šulga.** Self-assembly and interaction of nanostructures. Tartu, 2011, 114 p.
6. **Wojciech Kuznik.** Quantum-chemical computer simulations of the linear and non-linear optical properties of pyrazoloquinoline and dicyanopyrazine derivatives. Tartu, 2012, 89 p.
7. **Leonid Dorogin.** Structural and tribological properties of zero- and one-dimensional nanocrystals. Tartu, 2012, 193 p.
8. **Viljar Palmre.** Fabrication and characterization of microporous carbon-based electroactive polymer actuators. Tartu, 2012, 99 p.
9. **Madis Paalo.** Synthesis of CNT-metal oxide nanocomposites: sol-gel process, rheology, structural and functional properties. Tartu, 2014, 175 p.
10. **Raul Vålbe.** Development of ionic liquid composites by sol-gel method for elaboration of industrial nano- and microstructures. Tartu, 2014, 97 p.
11. **Urmas Joost.** Impurity and preparation dependent properties of titania thin films. Tartu, 2014, 155 p.
12. **Madis Umalas.** Application of sol-gel technology for production of ceramic nanocomposites and functional coatings. Tartu, 2015, 136 p.
13. **Elena Samsonova.** Energy transfer probe as a tool to study morphological and structural origins of fluorescence quenching in rare-earth doped nanophosphors. Tartu, 2015, 114 p.
14. **Jay Mondal.** Novel Corrosion Protective Nanostructured Composite Coatings. Tartu, 2016, 104 p.
15. **Kathriin Utt.** Metal oxide mesostructures for optical applications. Tartu, 2016, 88 p.
16. **Kaido Siimon.** Electrospun gelatin cross-linked by glucose. Tartu, 2016, 84 p.
17. **Marko Part.** Combined three-dimensional sol-gel structures and atomic layer deposited thin films. Tartu, 2017, 162 p.
18. **Pejman Rasti.** Analysis of Remote Sensing Image Super Resolution using Fluid Lenses. Tartu, 2017, 188 p.
19. **Ivo Romet.** Recombination luminescence of doped borates: origin and application prospects in dosimetry. Tartu, 2017, 111 p.

20. **Vladimir I. Kondratiev.** Processing and characterization of transparent electrode materials. Tartu, 2017, 111 p.
21. **Taivo Jõgiaas.** Mechanical properties of atomic layer deposited thin films and nanocomposites. Tartu, 2017, 125 p.
22. **Lauri Aarik.** Atomic layer deposition and characterization of thin oxide films for application in protective coatings. Tartu, 2017, 180 p.
23. **Triin Kangur.** Preparation and functional properties of stochastic micro-structured sol-gel silica materials. Tartu, 2018, 96 p.